



**HAL**  
open science

## Large-Eddy Simulation of the lean-premixed PRECCINSTA burner with wall heat loss

Pierre Bénard, G. Lartigue, Vincent Moureau, Renaud Mercier

► **To cite this version:**

Pierre Bénard, G. Lartigue, Vincent Moureau, Renaud Mercier. Large-Eddy Simulation of the lean-premixed PRECCINSTA burner with wall heat loss. Proceedings of the Combustion Institute, 2019, 37 (4), pp.5233-5243. 10.1016/j.proci.2018.07.026 . hal-02105031

**HAL Id: hal-02105031**

**<https://hal.science/hal-02105031>**

Submitted on 26 Nov 2020

**HAL** is a multi-disciplinary open access archive for the deposit and dissemination of scientific research documents, whether they are published or not. The documents may come from teaching and research institutions in France or abroad, or from public or private research centers.

L'archive ouverte pluridisciplinaire **HAL**, est destinée au dépôt et à la diffusion de documents scientifiques de niveau recherche, publiés ou non, émanant des établissements d'enseignement et de recherche français ou étrangers, des laboratoires publics ou privés.

## **Large-Eddy Simulation of the lean-premixed PRECCINSTA burner with wall heat loss**

Pierre Benard, G. Lartigue, V. Moureau, Renaud Mercier

► **To cite this version:**

Pierre Benard, G. Lartigue, V. Moureau, Renaud Mercier. Large-Eddy Simulation of the lean-premixed PRECCINSTA burner with wall heat loss. Proceedings of the Combustion Institute, Elsevier, 2019, 37 (4), pp.5233-5243. 10.1016/j.proci.2018.07.026 . hal-02105031

**HAL Id: hal-02105031**

**<https://hal.archives-ouvertes.fr/hal-02105031>**

Submitted on 26 Nov 2020

**HAL** is a multi-disciplinary open access archive for the deposit and dissemination of scientific research documents, whether they are published or not. The documents may come from teaching and research institutions in France or abroad, or from public or private research centers.

L'archive ouverte pluridisciplinaire **HAL**, est destinée au dépôt et à la diffusion de documents scientifiques de niveau recherche, publiés ou non, émanant des établissements d'enseignement et de recherche français ou étrangers, des laboratoires publics ou privés.

# Large-Eddy Simulation of the lean-premixed PRECCINSTA burner with wall heat loss

P. Benard<sup>a,\*</sup>, G. Lartigue<sup>a</sup>, V. Moureau<sup>a</sup>, R. Mercier<sup>b</sup>

<sup>a</sup> Normandie Univ, INSA Rouen, UNIROUEN, CNRS, CORIA, 76000 Rouen, France

<sup>b</sup> SAFRAN Tech, Rue des Jeunes Bois, Châteaufort - CS 80112, 78772 Magny-les-Hameaux, France

---

## Abstract

Swirl burners are widely used in aeronautical engines and industrial gas turbines. These burners enhance the flame stabilization by bringing back hot products to the reactive zone and their topology ensures a good compactness. However, the outer recirculation zones created in these burners induce wall heat loss that affects the flame structure. This paper proposes a numerical strategy based on Large-Eddy Simulation (LES) and non-adiabatic boundary conditions with a skeletal chemistry approach coupled to the Dynamic Thickened Flame model (TFLES). Simulations were performed on the PRECCINSTA burner with meshes up to 877 millions elements. Results demonstrated the impact of the addition of wall heat loss on the lift-off of the external flame front, leading to a flame topology change from a M-shape to a V-shape. This lift-off height increases with the grid resolution showing the strong influence of the mesh resolution on the flame topology. Comparisons of the non-adiabatic LES results on the finest mesh with the experimental data show an unprecedented agreement. The flame quenching process is analyzed and exhibits the role of strain rate which controls the level of penetration of cooled products within the inner reaction zone.

## Keywords:

non-adiabatic premixed combustion, swirl burner, Large-Eddy Simulation, heat loss, skeletal chemistry

---

---

\*Corresponding author

Email address: pierre.benard@coria.fr (P. Benard)

## 1. Introduction

Swirl-type combustion is widely used for industrial burners as it provides several advantages. When the geometrical swirl number is high enough, i.e. over 0.6, the burner exhibits a Central Recirculation Zone (CRZ) and Outer Recirculation Zones (ORZ). In these zones, hot burnt gases recirculate helping flame stabilization and extending flammability limits [1]. In premixed swirl burner, the flame structure is influenced by wall heat transfer [1]. Indeed, it has been observed that strong heat loss may influence the ORZ, weakening the stabilization process [2] up to local extinction [3].

Numerous numerical studies have been performed on the so-called PRECCINSTA burner [4], a swirl lean-premixed methane-air combustor. Most of them focus on Large-Eddy Simulations (LES) with adiabatic wall conditions. These computations were not able to correctly capture the flame structure. Moureau et al. [5] and Franzelli et. al. [6, 7] agree to attribute this effect to the adiabatic wall condition or to partial premixing without being able to validate it. However, these studies demonstrated the strong influence of the mesh resolution [5] and of the chemistry description [7] on the flow and the flame topology. Indeed, Franzelli et al. [7] explained the need of analytical or skeletal schemes to accurately predict the consumption speed, the intermediate species concentration and the flame structure.

In this paper, LES of the PRECCINSTA burner are carried out with a skeletal scheme using four different grid resolutions and with adiabatic and non-adiabatic wall conditions. The objective is to study grid resolution and heat loss influence on the flame structure and pollutant formation. First, the experimental set-up and the numerical modeling are presented, as well as the strategy established to obtain the non-adiabatic condition is exposed. Then, the LES results are analyzed and compared to experimental data.

## 2. Experimental set-up

Designed within the EU project PRECCINSTA, the combustor is derived from an industrial design by SAFRAN Helicopter Engines [4, 8], representative of a real aeronautical gas turbine combustor. It was widely studied experimentally [9] or numerically [5, 6, 10–14].

As described by Fig. 1, the geometry consists of three parts. The premixed methane-air mixture is injected into the plenum and swirled through the injector by twelve radial veins before entering the chamber through a converging nozzle with a central conical bluff-body. The chamber has a square cross-section of  $86 \times 86 \text{ mm}^2$

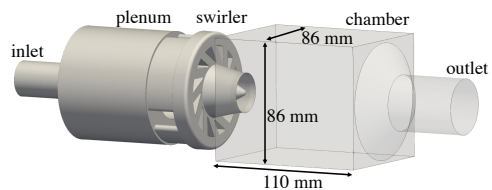


Figure 1: Computed geometry of the PRECCINSTA burner.

Air flow rate [g/min]	734.2
Methane flow rate [g/min]	35.9
Inlet temperature [K]	300.0
Thermal power [kW]	30.0
Equivalence ratio	0.83

Table 1: Flame parameters of the experimental case.

and a height of 110 mm. The burnt gases leave the burner by a cone-shaped exhaust pipe. 1.5 mm-thick quartz windows are placed on the combustor side walls to enable optical diagnostics. Laser Raman scattering was used to provide quantitative measurements of major species and temperature at different sections.

The present study focuses on the 30 kW “quiet” case at equivalence ratio 0.83 (see Tab. 1). Although air and methane are injected separately in the experiment, a perfectly premixed injection condition is assumed in this paper as in previous studies [5, 10, 12, 13]. At this specific operating conditions, Franzelli et al. [6] showed that this assumption has a negligible effect on the results. From Moureau et al. [5], the integral length scale is estimated as  $\ell_T = 7.0 \text{ mm}$  and the Kolmogorov length scale as  $\eta = 29 \mu\text{m}$ . The eddy turn-over time and the Precessing Vortex Core characteristic time scale have a similar value, around 2.0 ms, while the Flow Through Time is estimated around 30 ms.

## 3. Numerical modeling

Large-Eddy Simulations are performed using the in-house solver YALES2 [15]. This massively parallel finite-volume code solves the low-Mach number Navier-Stokes equations using a projection method [16] for variable density flows [17]. Density, momentum and scalar equations are solved using a 4th-order centered scheme in space and a 4th-order Runge-Kutta-like scheme in time [18]. It is able to handle unstructured meshes up to billions of elements.

Finite-rate chemistry is employed: all species appearing in the chemical mechanism plus the sensible enthalpy are transported. The source terms are evaluated

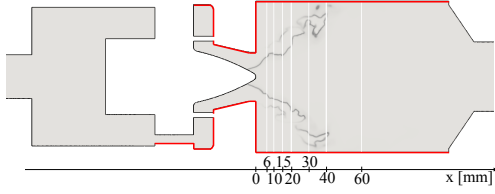


Figure 2: Adiabatic (red) and non-adiabatic (black) boundary condition for the non-adiabatic cases. Vertical white lines show the experimental temperature and species profiles.

from the kinetic mechanism at each control volume and for each time step. To avoid being limited by the chemical time step, an operator splitting method is used [19] relying on the stiff ODE solver CVODE [20]. A specific strategy to distribute the chemistry computation on all computing cores is adopted [21].

The kinetic scheme of Sankaran et al. [22] composed of 17 species and 73 reactions is used. This scheme is based on the GRI 1.2 mechanism [23] and dedicated to lean premixed methane-air combustion. Unstrained laminar 1D premixed flames were computed with YALES2 at the operating conditions from Tab. 1. The obtained laminar flame speed is  $s_L^0 = 0.302 \text{ m}\cdot\text{s}^{-1}$  and thermal flame thickness is  $\delta_L^0 = 473 \mu\text{m}$ .

Turbulent sub-grid scale (SGS) stresses are modeled with the localized dynamic Smagorinsky model [24]. The kinetic scheme is coupled with the DTFLES model [25] to resolve the flame front on the LES grid and to account for SGS turbulence/chemistry interactions using the efficiency function of Charlette [26] with the fractal parameter set to  $\beta = 0.5$ .

The flame sensor, which locally activates the flame thickening is defined according to [7]. It relies on the source term of a fictive progress variable based on CO, CO<sub>2</sub> and H<sub>2</sub>O:  $\dot{\omega}_c = \dot{\omega}_{\text{CO}} + \dot{\omega}_{\text{CO}_2} + \dot{\omega}_{\text{H}_2\text{O}}$ . The flame sensor is set to 1.0 when  $\dot{\omega}_c$  exceeds 10% of its maximum value for the unstrained laminar flame, and 0.0 elsewhere. A filtering operation is performed to smooth the flame sensor away from the 10% region. This modeling strategy has been validated on 1D unstrained laminar flame and classical 2D flame-vortex interactions cases.

Convective heat transfer through the injector system and quartz windows is modeled as a local temperature Dirichlet boundary condition. The wall temperature was not measured experimentally and was obtained here through a trial and error procedure based on non-adiabatic LES computations. The boundary condition was calibrated for mesh 2 and validated for mesh 3 (see Tab. 2). A first guess was designed from experimental data: water-cooling in the injector and natural con-

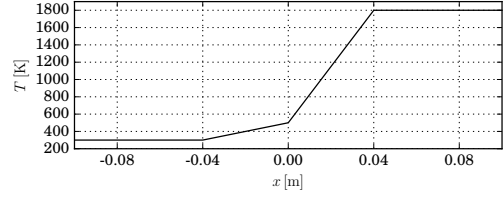


Figure 3: Wall temperature profile along the axial direction.

Mesh name	1	2	3	4
#Nodes [Million]	0.4	2.3	18.5	147
#Cells [Million]	1.7	14	110	877
$\Delta$ [mm]	1.2	0.6	0.3	0.15
$\ell_T/\Delta$	5.8	11.7	23.3	46.5
$\Delta/\eta$	41.4	20.7	10.3	5.1
$\delta_L^0/\Delta$	0.35	0.71	1.41	2.83
$\langle \max(\mathcal{F}) \rangle$	16.6	10.3	5.7	3.3

Table 2: Resolution parameters for the LES computational grids.

vection for lateral walls. Then, seven temperature profiles were necessary to achieve the final results. The cost function of the optimization process was based on the temperature in the corner recirculation zones and the maximum CO mass fraction in the outer branch. It was found that almost no heat loss appear on the injector nozzle but mainly on the combustion chamber base, due to the swirler water cooling system, and quartz windows. As illustrated by Fig. 2, the nozzle is considered adiabatic, and heat transfer occurs at the external wall of the injector, the chamber base and the chamber lateral walls. The final wall temperature condition is shown in Fig. 3.

A slight preheating of the methane-air mixture was observed experimentally. This preheating is reproduced in the simulation by the heat transfer in the swirler. As a result, the temperature reaches values between 320 K and 380 K before entering the combustion chamber [8]. In this study, the preheating in the injector due to wall temperature profile induces an increase of the mean temperature to 320.5 K, which is interestingly the same as previous LES studies [6, 14], which imposed the fresh gases temperature at 320 K.

For the considered burner, LES is performed successively on meshes with 0.4, 2.3, 18.5, and 147.2 million nodes with the strategy developed in [5]. The grid size  $\Delta$  in the flame region and the ratios of the turbulence and flame length scales [5] are presented in Tab. 2.

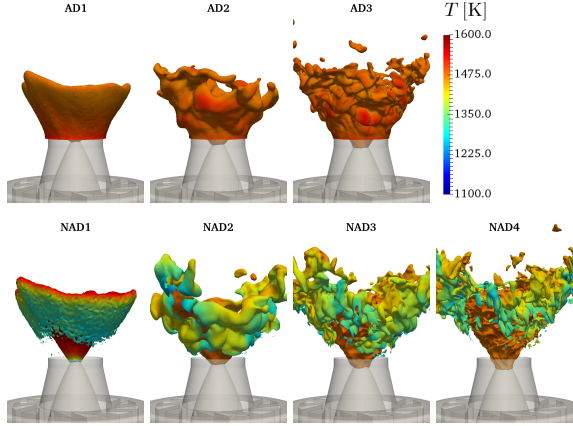


Figure 4: Normalized progress variable iso-contour  $c = 0.7$ , conditioned to heat release rate values exceeding 1% of its maximum value, colored by the temperature.

#### 4. Results and discussion

All the performed LES computations are listed in Tab. 3, combining the different meshes and wall thermal conditions. As shown in Tab. 2, the time-averaged maximum value of the thickening factor  $\mathcal{F}$  decreases at each grid refinement. However, even with the most refined mesh composed of 877 million elements, the SGS flame-turbulence interaction model is still necessary but is expected to have a very small impact on the results. A maximum thickening of around 3 means that the equivalent laminar non-thickened flame is resolved with a grid spacing of  $50 \mu\text{m}$ . At this resolution, the relative error on the laminar flame speed is less than 0.5% and species profiles are correctly reproduced.

The non-adiabatic cases present different wall heat loss amplitude as revealed by Tab. 3. The integral of the heat flux on the walls for the NAD2, NAD3 and NAD4 cases show a similar amplitude, around 1800 W, while it is underestimated of 80% for the NAD1 case, due to the poor resolution.

The flame structure is illustrated in Fig. 4 via an iso-contour of the normalized progress variable  $c = 0.7$  where the heat release rate exceeds 1% of its maximum value. With the coarsest mesh and adiabatic condition, the flame surface does not exhibit resolved wrinkling. As the resolution increases, resolved wrinkling appears and pockets of reactants detach from the flame front. The flame presents an M-shape structure with an internal flame attached to the nozzle and an external front attached to the chamber base.

Figure 5a compares the time-averaged temperature profiles obtained on all meshes to the experiment at

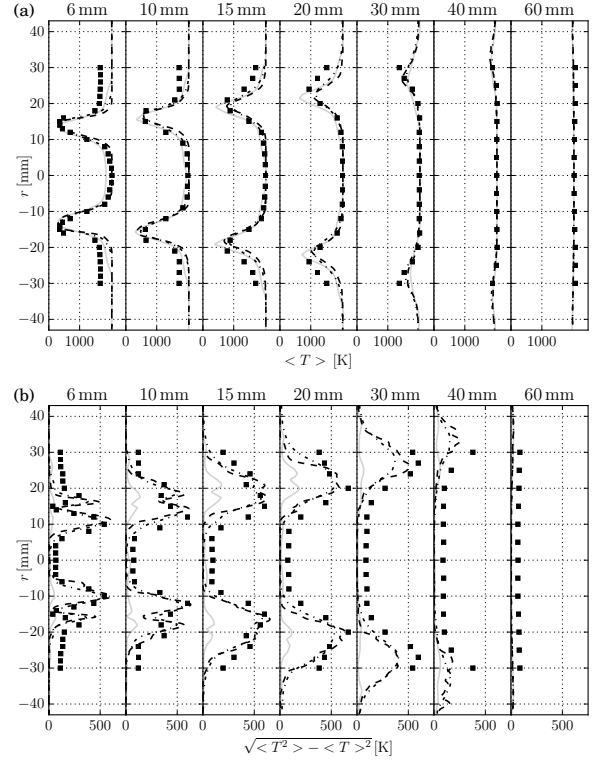


Figure 5: Mean (a) and RMS (b) temperature profiles for AD1 (—), AD2 (---), AD3 (---) cases and experiment (■).

seven sections in the combustion chamber. The LES computations AD2 and AD3 correctly reproduce the CRZ and the flame front, while the AD1 case underestimates the temperature in the CRZ due to the large thickening of the flame. The ORZ temperature is overestimated in all cases since wall heat loss is missing. On the RMS temperature profiles of Fig. 5b, the AD1 case exhibits very low dynamics. On the contrary, even if the AD2 and AD3 cases underestimate the fluctuations in the ORZ compared to the experimental data, they provide a good agreement elsewhere.

The comparison of time-averaged and RMS carbon dioxide ( $\text{CO}_2$ ) mass fraction profiles to the experiment in Fig. 7a and Fig. 7b reveals that the adiabatic condition is in good agreement with experiment. Only the RMS profiles of the AD1 case are far from the experimental data as for the temperature, due to lack of dynamics.

As illustrated by Fig. 4, when heat loss occurs, the temperature in the reaction zone ( $c = 0.7$ ) of the outer flame front lies between 1300 and 1500 K while 1550 K is found in the adiabatic cases. This is confirmed by the mean temperature profiles of Fig. 6a showing that,

Case name	AD1	NAD1	AD2	NAD2	AD3	NAD3	NAD4
Mesh	1	1	2	2	3	3	4
Thermal condition	AD	NAD	AD	NAD	AD	NAD	NAD
External flame lift-off height [mm]	-	1.9	-	3.3	-	5.3	25.7
Time-averaged heat losses [kW]	-	0.99	-	1.81	-	1.91	1.78
Physical time [ms]	34.9	47.6	83.9	83.6	51.7	51.3	33.4
CPU time [ $\times 10^5$ hCPU]	0.015	0.022	0.24	0.24	3.1	3.6	36.9

Table 3: Summary of all the LES cases. AD refers to adiabatic wall condition and NAD to non-adiabatic wall condition.

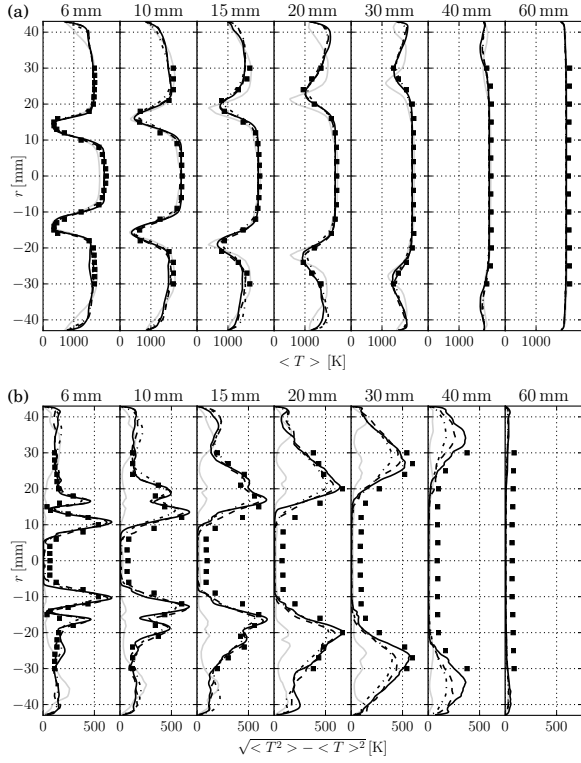


Figure 6: Mean (a) and RMS (b) temperature profiles for NAD1 (—), NAD2 (-·-·-), NAD3 (- - -), NAD4 (—) cases and experiment (■).

in addition to the CRZ and flame front area, the ORZ is well captured with a mean temperature around 1800 K at the first section  $x = 6$  mm, i.e. 200 K less than the adiabatic cases. The same trend is observed on RMS profiles of Fig. 6b: the fluctuations are correctly captured everywhere except for the NAD1 case. The addition of heat loss has a negligible effect on mean  $\text{CO}_2$  mass fraction profiles as shown by Fig. 8a. The RMS profiles of Fig. 8b indicate a slightly better prediction of  $Y_{\text{CO}_2}$  fluctuations in the ORZ part, compared to adiabatic cases.

The flame structure changes with the thermal wall

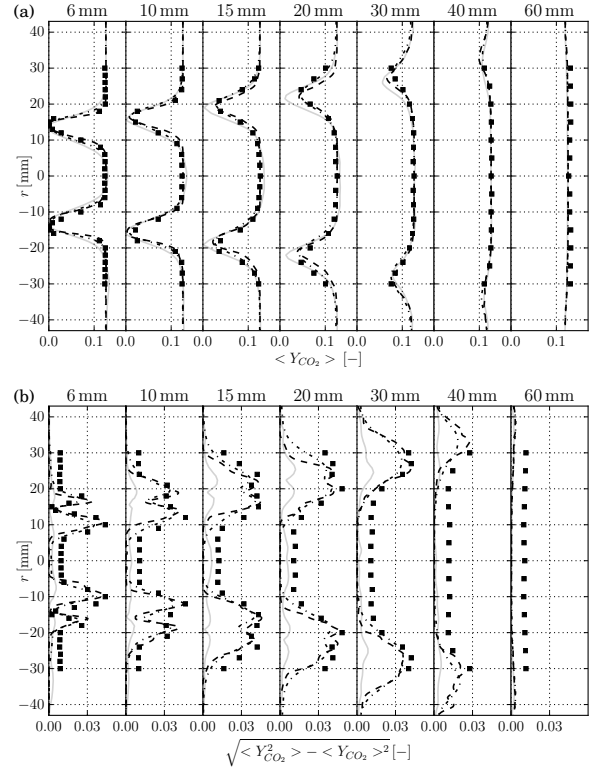


Figure 7: Mean (a) and RMS (b)  $\text{CO}_2$  mass fraction profiles for AD1 (—), AD2 (-·-·-), AD3 (- - -) cases and experiment (■).

condition. Figure 4 shows a detached external flame front in the non-adiabatic cases. The lift-off height was measured based on the time-averaged flame sensor, which is linked to the local maximum of heat release, and collected in Tab. 3. With the increase of the mesh resolution, the lift-off height (LOH) grows up from 1.9 to 25.7 mm, leading to a V-shape flame for NAD4.

This V-shape flame structure is observed experimentally as confirmed by the CO profiles shown in Figs. 9a and 10a. The adiabatic cases exhibit a double  $Y_{\text{CO}}$  peak on the first sections whatever the resolution, representa-

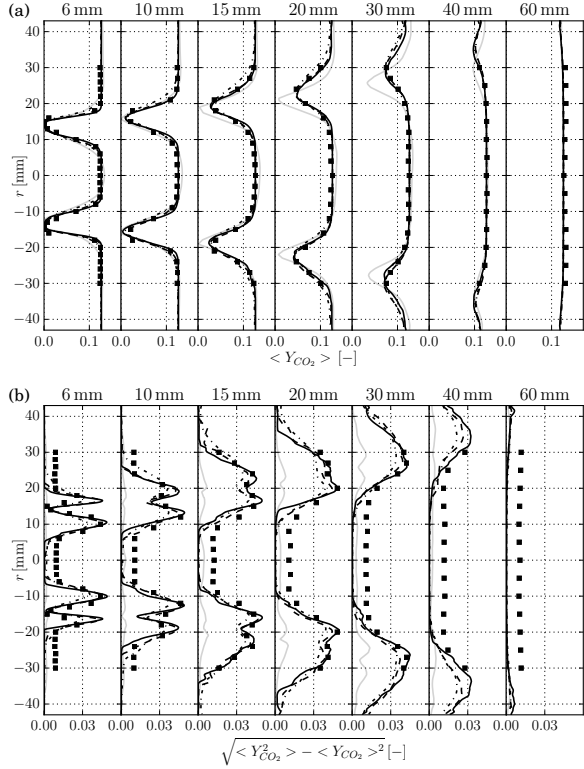


Figure 8: Mean (a) and RMS (b)  $CO_2$  mass fraction profiles for NAD1 (—), NAD2 (---), NAD3 (- · - ·), NAD4 (—) cases and experiment (■).

tive of a double flame front. Contrarily to the results of Franzelli et al. [6] in the same operating conditions, the use of a skeletal kinetic scheme here allows to capture the CO behavior. The addition of heat loss enables to annihilate the external flame front. The NAD4 case reproduces very well the experimental  $Y_{CO}$  profiles: only a slight overestimation is found in the ORZ. As the cell size increases, the  $Y_{CO}$  profiles increase globally. This is due to a known behavior of the TFLES turbulent combustion model: as the flame is thickened, the integral of intermediate species profile is artificially increased [27].

The  $Y_{CO}$  RMS profiles are plotted in Figs. 9b and 10b for the adiabatic and the non-adiabatic cases, respectively. In the adiabatic cases, except AD1, the experiment profiles are retrieved only for the inner flame. The dynamics in the non-adiabatic cases is well reproduced with less fluctuations for the outer flame front. NAD4 shows the best agreement to the experiment.

Figure 11 compares the OH-LIF measurements to instantaneous OH concentrations on AD3, NAD3 and NAD4 cases. It is observed that the intermediate species

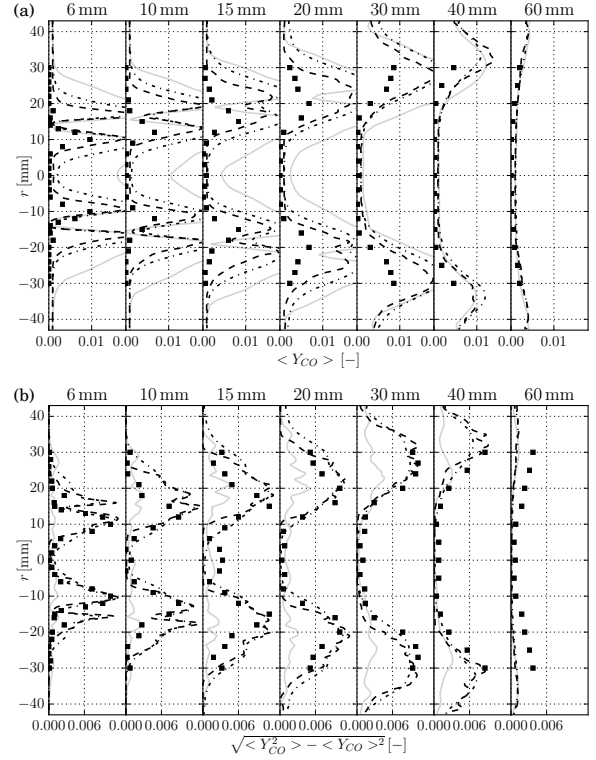


Figure 9: Mean (a) and RMS (b) CO mass fraction profiles for AD1 (—), AD2 (---), AD3 (- · - ·) cases and experiment (■).

OH is produced in the reaction zone and almost entirely destroyed in the post-flame area. In the non-adiabatic case, no gradient of the OH mass fraction is found in the ORZ as in the experiment. Moreover, the NAD4 case seems to have the best agreement in terms of flame wrinkling and spatial distribution of OH mass fraction gradient compared to the experiment.

The outer flame front extinction is now analyzed by introducing the local enthalpy defect  $\Delta H = H - H_{ad}$  where  $H$  and  $H_{ad}$  are the local total enthalpy and the total enthalpy of the adiabatic mixture, respectively. A 2-D longitudinal cut of the NAD4 case colored by the instantaneous value of  $\Delta H$  is shown in Fig. 12 and confirms that the slow characteristic time scale of the ORZ promotes heat exchange at the burner walls and causes a drastic fall of total enthalpy in this region. The impact of the enthalpy defect on the outer flame structure is analyzed in Fig. 13 by plotting, for the NAD4 case, a scatter-plot of the heat release rate  $\dot{\omega}_T/\mathcal{F}$  conditioned to  $c \in [0.75 - 0.8]$  against the velocity gradient norm  $|\nabla \mathbf{u}|$ . The velocity gradient is used here as an indicator of the local strain rate seen by the flame front and

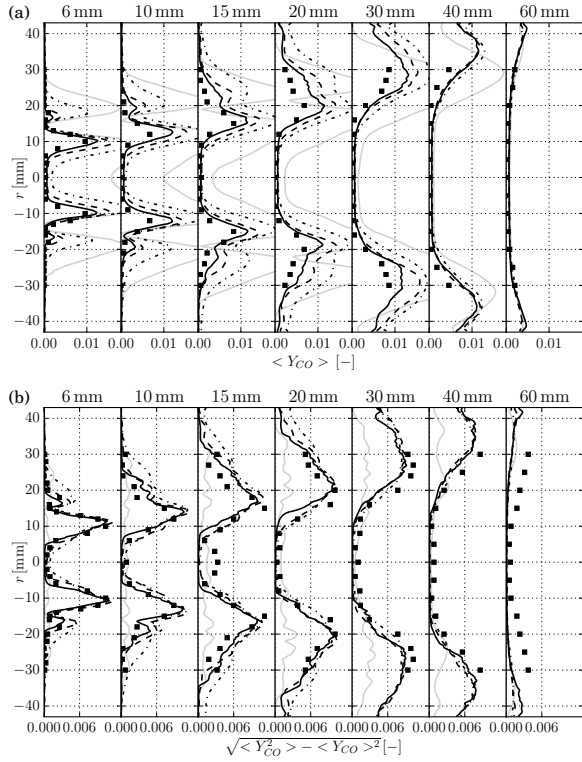


Figure 10: Mean (a) and RMS (b) CO mass fraction profiles for NAD1 (—), NAD2 (---), NAD3 (- · - ·), NAD4 (—) cases and experiment (■).

each point is colored by its local enthalpy defect. Red points corresponds to adiabatic zones while the level of heat loss increases for colors reaching dark blue. Three main zones can be identified: (i) A high density of red points (adiabatic) is located at high heat release rates ( $\dot{\omega}_T/\mathcal{F} > 2.10^9 \text{ W.m}^3$ ): they mainly belong to the internal flame front which remains adiabatic and correspond to  $|\nabla \mathbf{u}| \in [10000; 15000] \text{ s}^{-1}$ ; (ii) A low density of blue points (high enthalpy defect) is located at moderate heat release rates ( $\dot{\omega}_T/\mathcal{F} \in [1.10^9; 2.10^9] \text{ W.m}^3$ ): they correspond to the reactive outer flame front which is subjected to heat loss and a similar velocity gradient as the inner flame front; (iii) A high density of blue points (high enthalpy defect) is located at the bottom of the figure ( $\dot{\omega}_T \approx 0$ ) and corresponds to higher values of  $|\nabla \mathbf{u}| \in [10000; 40000] \text{ s}^{-1}$ : they correspond to the quenched outer branch where mixing between adiabatic fresh gases and cooled burnt gases occurs without chemical activity. Interestingly, for the same levels of  $\Delta H$  and  $c$ , (ii) and (iii) exhibit both reacting and quenched flame fronts suggesting that enthalpy defect is not the only physical phenomenon controlling the

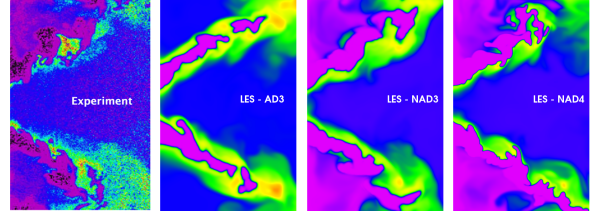


Figure 11: Comparison of OH - LIF measurements to instantaneous OH normalized concentration from LES cases. From left to right: experiment, AD3, NAD3 and NAD4 cases. Colormap: 0.0 0.25 0.5 0.75 1.0.

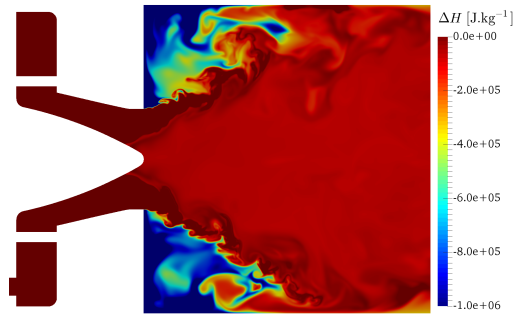


Figure 12: Instantaneous enthalpy defect on the mid-plane for NAD4.

flame quenching process. However, considering both strain rate (estimated here through  $|\nabla \mathbf{u}|$ ) and enthalpy defect  $\Delta H$  allows to clearly discriminate the reacting points with low strain rates (ii) and quenched points with higher strain rates (iii). The increase of the LOH shown in Tab. 3 is therefore due to higher resolved strain rates on the refined grids leading to an increase of the quenched flame surface. This conclusion is in line with previous studies performed on counterflow flame configurations [28] showing that burnt gases enthalpy defect decreases the resistance of premixed flame fronts to large strain rates.

## 5. Conclusions

In this work, a numerical strategy to take into account wall heat loss on the lean premixed methane-air PRECINSTA burner has been proposed. This methodology relies on high-fidelity LES, a skeletal kinetic scheme, the DTFLES model and a wall temperature Dirichlet boundary condition. The results were compared to adiabatic computations and to experimental data. Different grid resolutions were tested, with meshes containing from 1.7 up to 877 millions of elements. The results show that the flame structure is strongly affected by the

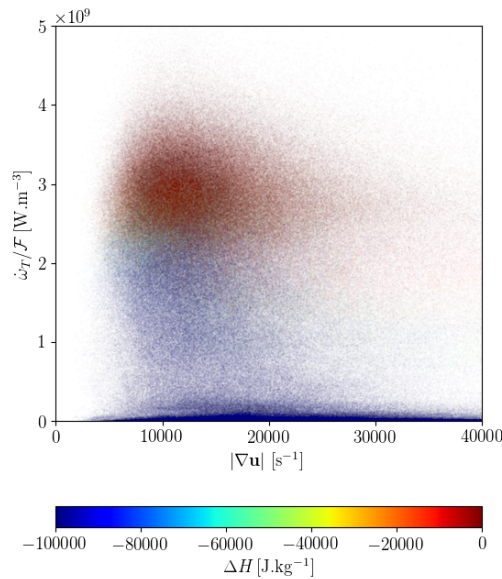


Figure 13: Scatter plot of the heat release rate against the velocity gradient norm, for points with  $c \in [0.75-0.8]$ , colored by the enthalpy defect for NAD4 simulation.

wall heat transfer whatever the grid size. The enthalpy defect in burnt gases enhances the sensitivity to local strain rate leading to quenching of the outer flame front and changing the flame topology to a V-shape. The temperature and CO distributions are then highly affected. The non-adiabatic case with the most refined grid shows the best agreement to experimental results. Indeed, the V-shape flame structure, the front wrinkling, the temperature and species profiles as well as OH distribution are recovered, confirming the importance of taking into account wall heat loss and complex chemistry effects in such configuration. These results may further be used to develop a sub-grid model closure able to accurately capture intermediate species.

## Acknowledgments

This work was granted access to the HPC resources from CINES under the allocations A0032B06880 made by GENCI and from CRIANN under the allocation 2012006.

## References

- [1] T. Poinso, D. Veynante, *Theoretical and numerical combustion*, RT Edwards, Inc., 2005.
- [2] N. Syred, J. Beer, *Combust. Flame* 23 (2) (1974) 143–201.

- [3] R. Mercier, P. Auzillon, V. Moureau, N. Darabiha, O. Gicquel, D. Veynante, B. Fiorina, *Flow, Turbul. Combust.* 93 (2014) 349–381
- [4] G. Lartigue, U. Meier, C. Berat, *Appl. Therm. Eng.* 24 (11) (2004) 1583–1592.
- [5] V. Moureau, P. Domingo, L. Vervisch, *Combust. Flame* 158 (7) (2010) 1340–1357.
- [6] B. Franzelli, E. Riber, L. Y. M. Gicquel, T. Poinso, *Combust. Flame* 159 (2) (2012) 621–637.
- [7] B. Franzelli, E. Riber, B. Cuenot, *C. R. Mec.* 341 (1-2) (2013) 247–256.
- [8] W. Meier, P. Weigand, X. R. Duan, R. Giezendanner-Thoben, *Combust. Flame* 150 (1-2) (2007) 2–26.
- [9] P. Weigand, X. R. Duan, W. Meier, U. Meier, M. Aigner, C. Brat, *Proc. of the European Combustion Meeting*, 2005, p. 235.
- [10] S. Roux, G. Lartigue, T. Poinso, U. Meier, C. Brat, *Combust. Flame* 141 (1-2) (2005) 40–54.
- [11] V. Moureau, P. Minot, H. Pitsch, C. Brat, *J. Comput. Phys.* 221 (2) (2007) 600–614.
- [12] B. Fiorina, R. Vicquelin, P. Auzillon, N. Darabiha, O. Gicquel, D. Veynante, *Combust. Flame* 157 (2010) 465–475.
- [13] P. Wang, J. Frhlich, U. Maas, Z. Hea, C. Wang, *Combust. Flame* 164 (2016) 329–345.
- [14] J. M. Lourier, M. Sto hr, B. Noll, S. Werner, A. Fiolitakis, *Combust. Flame* 183 (2017) 343–357.
- [15] V. Moureau, P. Domingo, L. Vervisch, *C. R. Mec.* 339(2/3) (2-3) (2011) 141–148.
- [16] A.J. Chorin, *Math. Comp.* 22 (1968) 745–762.
- [17] C. D. Pierce, P. Moin, *J. Fluid Mech.* 504 (2004) 73–97.
- [18] M. Kraushaar, Ph.D. thesis, CERFACS (2011).
- [19] R. Yu, J. Yu, X.-S. Bai, *J. Comput. Phys.* 231 (16) (2012) 5504–5521.
- [20] S. D. Cohen, A. C. Hindmarsh, *Comput. Phys.* 10 (2) (1996) 138–143.
- [21] P. Benard, V. Moureau, G. Lartigue, Y. DAngelo, *Int. J. Hydrogen Energy* 42 (4) (2017) 2397–2410.
- [22] R. Sankaran, E.R. Hawkes, J.H. Chen, T. Lu, C.K. Law, *Proc. Combust. Inst.* 31 (2007) 1291–1298.
- [23] G. Smith, D. Golden, M. Frenklach, N. Moriarty, B. Eiteneer, M. Goldenberg, C. Bowman, R. Hanson, S. Song, W. Gardiner, et al., *Technical Report*, Gas Research Institute (1999).
- [24] M. Germano, U. Piomelli, P. Moin, W. H. Cabot, *Phys. Fluids A* 3 (7) (1991) 1760–1765.
- [25] O. Colin, F. Ducros, D. Veynante, T. Poinso, *Phys. Fluids* 12 (7) (2000) 1843–1863.
- [26] F. Charlette, C. Meneveau, D. Veynante, *Combust. Flame* 131 (2002) 181–197.
- [27] M. Cailler, R. Mercier, V. Moureau, N. Darabiha, B. Fiorina, 55th AIAA Aerospace Sciences Meeting, AIAA 2017-0606 (2017).
- [28] B. Coriton, M.D. Smooke, A. Gomez, *Combust. Flame* 157 (11) (2010) 2155–2164

*In black, referees questions, comments and queries;  
in blue, replies to referees;  
in red, changes made to the paper.*

## **Reply to referees and modifications made to the manuscript “Large-Eddy Simulation of the lean-premixed PRECCINSTA burner with wall heat loss” by P. Bénard et al.**

### **Reviewer #1: Very Good**

The authors are grateful for the careful analysis of the referee. Please find below the answers to the referee's remarks and the changes brought to paper to prepare the revised version.

*This papers aims to show the impact of wall heat loss on the flame topology of the well-known methane-air swirled PRECCINSTA burner. After a brief review of the results obtained in the community on this configuration, the experimental setup is recalled and the numerical setup is described in terms of mesh resolution, numerics, boundary conditions as well as chemistry and subgrid modeling. Differences between adiabatic and non-adiabatic simulations are then discussed, focusing on instantaneous flame topology, profiles of mean and RMS temperature, CO<sub>2</sub> and CO mass fractions. Finally, the impact of wall heat loss on the flame topology is shown, demonstrating that wall heat loss many affects the outer flame region.*

*Although widely studied experimentally and numerically, to the knowledge of the reviewer, no one has never shown very accurate numerical results neither for the outer flame region nor for the CO profiles. For the first time, this work gathers both an accurate numerical setup based on a 4th order convective scheme and a mesh resolution not so far from DNS and a detailed modeling approach (skeletal mechanism for methane-air combustion, thickened-flame approach for subgrid flame-turbulence interaction and non-adiabatic walls) able to accurately reproduce all the features of the reacting flow. Moreover, the paper is well-organized, well written and the analysis of the results compared to measurements helps to answer unresolved questions concerning CO profiles for instance. For all these reasons, I recommend this paper for presentation and publication to the Symposium of Combustion.*

*Minor comments:*

*- p6: flame sensor: it seems that depending on the groups using the thickened-flame approach, the definition of the flame sensor as well as the smoothing strategy vary significantly. The authors claim the modeling approach has been validated in canonical cases, it would have been interesting to add one example in this paper, or to have a reference to quote.*

*The flame sensor definition used in the thickened flame model has been validated on premixed unstrained 1D flames and classical 2D flame-vortex case of the PhD thesis of Benard, 2015.*

*Supplementary material on this topic is added to the revised version.*

*- p7 wall temperature profile: as wall temperature measurements were not conducted, the*

In black, referees questions, comments and queries;  
in blue, replies to referees;  
in red, changes made to the paper.

*authors used an iterative procedure to define the wall temperature boundary condition on the injector, chamber base and chamber walls. First, on which mesh was this procedure used? I suspect Mesh 2 has been used, as Mesh 1 shows very poor agreement with measurements. Moreover, it is said that the wall temperature has been adapted to match the experimental temperature and species. Which experimental points have been considered? Only the first experimental point or a region close to the wall? Such details should be added to the manuscript.*

The wall temperature strategy was calibrated on M2 and validated on M3. A first guess was designed from experimental data: water-cooling in the injector and natural convection for lateral walls. Then, seven temperature profiles were necessary to achieve the final results. The cost function of the optimization process was based on the temperature in the corner recirculation zones and the maximum CO mass fraction in the outer branch. This point will be further detailed in the revised version.

These details are added to the revised version and thermal power balance is included as Supplementary Material.

*- Figs 4,6,7,8,9, 10, 11: the choice of color for AD1 and NAD1 simulations make the relative curves very difficult to distinguish, the color scale should be modified. I'm not sure that the results for mesh1 are necessary in this paper. The mesh is very coarse, leading to numerical results far from the measurements. Skipping mesh1 would also make all the figures showing mean and RMS profiles clearer.*

The figures are enlarged and improved in the revised version.

*- again - Figs 4,6,7,8,9, 10, 11: the authors should choose between top and bottom and a) and b) for the mean and RMS profiles respectively. It is a) and b) in the figures themselves and in the text but top and bottom in the legends.*

This mismatch between figures and legends is corrected in the revised version.

*- Figs 6 and 7: the non-adiabatic LES show impressive agreement with the measurements for all the variables and at all the sections. Still, there is a difference on the RMS temperature profiles, where the simulations show almost zero fluctuations in the CRZ compared to the measurements, whatever the mesh resolution. Could the authors comment on that point?*

Experimental RMS temperature statistics as well as species concentration always show a minimum value while no fluctuations can be found in the LES, whatever the mesh resolution. This is also observed in the other numerical investigations with a different combustion model [Mercier et al., PCI 2015], a different code [Roux et al. 2005] and different injection strategies [Franzelli et al. 2007]. This behavior may be linked to experimental signal-to-noise ratio or low-frequency fluctuations of the operating conditions.

*- p13 : Comments on the effect of chemistry on CO profiles should be moderated. Looking on the results of Franzelli et al. who used an intermediate grid between Mesh 1 and Mesh2, adiabatic walls and a more reduced chemical scheme, using a skeletal mechanism does not improve much the results. It seems that using non-adiabatic walls is the key point to correctly reproduce the mean CO profiles, the impact of the chemical scheme being more limited*

The authors agree with the reviewer about the fact that non-adiabatic condition is the key point to specifically reproduce the CO profiles. A more reduced and well-tailored kinetic scheme may be able to retrieve these profiles. The same temperature boundary condition was used by

In black, referees questions, comments and queries;  
in blue, replies to referees;  
in red, changes made to the paper.

another team with a virtual optimized chemistry approach [Cailler et al., PCI 2017] with very good agreement in the non-adiabatic case [Maio et al., submitted for PCI 2019].

### **Reviewer #2: Very Good**

We thank the referee for his supporting review, please find below replies to his remarks and changes made to the paper accordingly.

*This is an very good paper describing LES results of lean premixed generic combustor. The authors have performed several LES simulations on different grids with resolution which differ order of magnitudes, with and without wall heat los. They adopted an approach using a reduced (but still detailed) chemistry, coupled with a Dynamic Thickened Flame model. It has been demonstrated that including heat loss is required to get good results for temperature and major species.*

*The results also demonstrate that the ATF closure is performing very well with regarding turbulent flame propagation speed; the turbulent flame propagation speed is independent on the grid spacing. Apart from the results on the coarsest grid, the temperature results on the other grids are very similar, and compare well with the experimental results (Figure 7 of the paper). On the other hand, from Figure 10, it can be seen that the CO (and OH) results depends strongly on the grid resolution. This, implies that for the intermediate species a sub-grid model closure is required. The authors already observe that the level of wrinkling depends on the grid solution, therefore should also draw the conclusion that this implies that a sub grid "wrinkling or pdf model" is required for accurate prediction of intermediate species.*

*A few minor comments:*

*In general the pictures are too small.*

*The figures are enlarged and improved in the revised version.*

*Some more explanation of the determined lift-off height is required, supported by a contour plot of temperature and/or the flame sensor. They mention that the LOH increases from 2.1 to 24.1 mm. However, that cannot be concluded from the temperature plots: they are (except for the very coarse grid), almost independent of the grid.*

*The lift-off height was not based from the temperature profile as wall heat loss are involved but taken as 1% of the time-averaged CO mass fraction.*

*New values obtained from the flame sensor were added to the revised version.*

### **Reviewer #3: Marginal**

We thank this referee for his careful analysis of the manuscript. Please find below the answers to his remarks and the changes brought to paper to prepare the revised version.

*Here, the authors apply finite rate chemistry LES using skeletal reaction mechanism and two wall temperature boundary conditions and tree/four grids to study the PRECCINSTA combustor. The results support other computational investigations in demonstrating that the thermal wall boundary condition is important for not only the flow but also for the flame topology and its*

In black, referees questions, comments and queries;  
in blue, replies to referees;  
in red, changes made to the paper.

dynamics. The results also demonstrate the influence of grid resolution on the flow and the flame.

*This paper is reasonably well written, covers an important topic of combustion LES evaluation and validation for simplified gas turbine combustor applications but is unfortunately not novel. Conventional combustion LES models are employed on three/four grids together with a skeletal methane-air reaction mechanism. Comparison is made with a fraction of the available experimental data. The only non-conventional aspect of the study is that the authors have tested two wall temperature profiles: adiabatic and non-adiabatic with an ad-hoc prescribed combustor wall temperature. This is well known to significantly influence the flow and the flame. The authors have not described how this wall temperature profile was arrived at besides using trial-and-error. This means that they have varied the profile until better agreement with the experimental data was achieved compared to the adiabatic profile - not a very scientific approach. Besides that I am very surprised about the grid sizes required to get good agreement with the experimental data - approximately ten times finer grids than anyone else. This is highly surprising and must be considered an outlier. The paper is rather weak in terms of analyzing the flame structure, and most of the results achieved are well known and are supported by other investigations. All in all, this makes the paper below or just average for inclusion in the Proceedings of the Combustion Institute. Additional issues includes:*

*o As mentioned in the Introduction, numerous numerical studies have been performed on the so-called PRECCINSTA burner. An unacceptably limited set of the available studies on this burner has been mentioned in the Introduction. Research outside of this selected group of authors has made valuable contributions that the authors should consider. This comment extends also to the list of simulations in Section 2.*

To their knowledge, the authors made reference to most of the publications about the simulations of the PRECCINSTA burner at the 'quiet' operating conditions (equivalence ratio of 0.83). The reference to the recent article of Wang et al. (2016) is added to the revised version as it provides the equivalent adiabatic numerical set-up with the same results on the external flame front and CO prediction. The past articles of Albouze et al. (2009) and Galpin et al. (2008) are not cited as they don't bring more insights to this study.

The reference to the article of Wang et al. (2016) is added in the revised version.

*o Figure 1 is too small, it should be extended to a full column with of 74 mm. The font size should also be enlarged to comply with the author instructions.*

It has been corrected in the revised version.

*o To facilitate the understanding of the combustor, the authors should make an effort to illustrate where the fuel is injected.*

As specified in the text, the fuel is injected perfectly mixed with the air into the plenum by the inlet.

*o Fig. 1 can also be found in Ref. [5] and either do the authors refer to that paper in the figure caption or do they replace this figure with a different one.*

In black, referees questions, comments and queries;  
in blue, replies to referees;  
in red, changes made to the paper.

The figure 1 describing the burner geometry was taken from Ref. [5] for which the first author is one of the co-authors of the present article. Moreover, the editor Elsevier is the same between 'Combustion & Flame' and 'Proceedings of the Combustion Institute' journals.

Nevertheless, the figure was rebuilt from scratch for the revised version to avoid any conflict.

*o In Section 2 the authors write: "Although air and methane are injected separately in the experiment, a perfectly premixed injection condition is assumed in this paper as in previous studies [5, 10, 12]. At this specific operating conditions, Franzelli et al. [6] showed that this assumption has a negligible effect on the results." I am not convinced that this is an appropriate assumption, and after consulting Franzelli et al. [6] and other numerical studies of the same combustor, not relying on this assumption and not cited by the authors, I become even more convinced that all twelve fuel injectors should be explicitly incorporated.*

To the knowledge of the authors, the non-perfectly premixed condition was only tested by Franzelli et al. and showed a negligible effect at this specific operating condition but appeared to impact the flame topology at equivalence ratio 0.7. To the authors' point of view, this assumption remains acceptable.

*o Using a low Mach number solver for this combustor is not a very good idea. Although the study considers the quiet flame at  $\phi=0.83$  thermoacoustic fluctuations occurs and may influence the flow and flame behavior.*

The quiet flame case exhibits no acoustics as the pressure drop fluctuations at the swirler are less than 4% [Meier et al. 2007, Roux et al. 2005], which is supported by the comparison of the flame wrinkling in instantaneous OH-LIF images [Fig. 12]. This quiet flame case can thus be computed with a low-Mach number solver as done by several other teams (Wang et al., 2016).

*o The reaction mechanism used is a skeletal reaction mechanism developed by Sankaran et al., 2007 from GRI-1.2 using sequential application of directed relation graph sensitivity analysis and computational singular perturbation. The resulting mechanism is said to be optimized for atmospheric conditions and lean conditions. As we now know, the reaction mechanism is crucial to successful LES and DNS computations. Neither in the original paper by Sankaran et al or in this paper is the reaction mechanism compared with experimental flame data or with detailed reaction mechanisms. I forcefully recommend the authors to extend the manuscript with such a comparison, including the ignition delay time, laminar flame speed, flame temperature, extinction strain rate and key species. This comparison can be included as supplementary material. A potential problem with this mechanism is that since fuel is separately injected, some burning may occur well outside of the regimes for which the mechanism is developed. Moreover, the skeletal mechanism is not well-suited for ignition according to Sankaran et al.*

The Lu17 mechanism with 73 reactions is already one of the largest mechanisms (with the DRM19 mechanism used by Lourier et al., 2017) used to simulate this semi-industrial burner. It was chosen for its performances for predicting finite-rate chemistry effects [Sankaran et al., 2007]. Derived from GRI-1.2 mechanism, Lu17 has been validated on PSR and auto-ignition at atmospheric pressure, equivalence ratio from 0.6 to 0.9 and low to moderate temperature range which is in line with the operating conditions of the present study. The laminar flame speed and thickness for 1D laminar flames have also been verified.

*o Using the (dynamic) Smagorinsky model does not allow for anisotropic subgrid flow features*

In black, referees questions, comments and queries;  
in blue, replies to referees;  
in red, changes made to the paper.

*and is associated with rather severe issues of excessive values of the subgrid viscosity. Often windowing of some sort is used to cure these problems. Suggest that the present description is elaborated on to cover these aspects.*

The dynamic Smagorinsky model has proven to give good results in this particular geometry [Moureau et al., C&F 2011] and the turbulent viscosity values on the finest mesh are very small ( $\mu_t/\mu < 5$ ).

*o How is the near-wall flow physics handled? The (dynamic) Smagorinsky model is not well suited to handle this unless a DNS grid or some ad hoc damping is applied.*

The walls are treated as no-slip conditions and no specific damping was adopted. The near-wall resolution lead to fully resolved wall boundary layer for the most refined meshes.

*o All figures are very small with a too small font size and line styles that are very difficult to separate from each other. This makes the paper challenging to read. For example, in Figs 6 to 11 it is virtually impossible to differentiate between the different simulation results. This must be corrected.*

The figures are enlarged and improved in the revised version.

*o Where does the flame sensor enter the modeling? This is unclear and appears ad-hoc.*

Details about the flame sensor were given to Reviewer #1 answers and Supplementary Material associated to the revised version provides flame sensor validation cases. The flame sensor is used to locally identify the thickening area for the TFLES turbulent combustion model.

*o The process of obtaining the final wall temperature profile was based on a trial-and-error procedure. Can the authors provide some information about how this was done, and most interestingly what is the sensitivity to the wall temperature profile along the combustor?*

See Reviewer #1 answers. Apart from NAD1 case, the non-adiabatic results present the same level of wall heat losses power.

Thermal power balance of all the LES cases is given as Supplementary Material.

*o The result section systematically excludes comparison of the axial, radial and azimuthal velocity components and their rms fluctuataions. This should be included. Moreover, to help assess the importance of grid resolution vs. that of the assumed wall temperature profile it is strongly recommended that the authors also include mean and rms velocity comparisons from the non-reacting LES computations.*

No velocity measurements are available at these operating conditions but at equivalence ratio 0.75. Such measurements were performed for other conditions.

*o The structure of the flame shown in Fig. 5 and briefly described deserves a more thorough presentation and discussion. We see that there are large differences between the seven flames due to the assumed wall temperature boundary condition and the grid but these are not discussed. Please extend the paper with such a discussion.*

The instantaneous snapshots representing the flames showed in Fig. 5 are analyzed with quantitative results given after.

*In black, referees questions, comments and queries;*  
*in blue, replies to referees;*  
*in red, changes made to the paper.*

*o Since a skeletal reaction mechanism is used the authors have access to the intrinsic flame structure and how it is affected both by the grid resolution and by the assumed wall temperature boundary condition. Please use this opportunity to discuss this very important aspect.*

The influence of the kinetic scheme on the intrinsic flame structure is out of the scope of this study but would deserve more analysis in a further article.

*o Figs. 6 to 11 are, as mentioned above, very difficult to decipher due to poorly chosen line styles, small figures and small font sizes. However, after zooming in significantly some details are starting to emerge: (i) the experimental data appears mirrored - this needs to be explained; (ii) the convergence seems non-monotonic with respect to grid resolution - this needs to be explained; (iii) the LES predictions result in asymmetric mean and rms profiles probably due to insufficient time-averaging - this needs to be discussed; and (iv) it is difficult to compare profiles with the two different wall boundary conditions since they appear in different figures.*

The experimental data are mirrored as it is usually done for this kind of comparison. The convergence is clearly non-monotonic as the flame wrinkling evolves, leading different flame topology. The LES results reveal some slight asymmetry, mostly for NAD4 case, due to insufficient time-averaging but the authors preferred showing these results, in line with the experiment, compared to axisymmetric averaged ones. This effect does not affect the performed analysis and the inferred conclusions.

*o Based on the comparison between the two families of LES predictions, using adiabatic and non-adiabatic wall temperatures, respectively, there are no clear evidence of one boundary condition being better than the other. The main reason for this is that there is no experimental data close enough to the wall to illustrate this.*

The authors are very surprised by this comment. 200K temperature difference is found between the adiabatic and non-adiabatic conditions on Outer Recirculation Zone. The non-adiabatic results show a clear better agreement to the experiment data. The authors agree that this study would benefit from experimental wall temperature measurements. Nevertheless, this kind of data were only produced in recent studies (Dem et. Al., 2015) for different operating conditions (equivalence ratio 0.9).

*o A very challenging question is why these simulations need more than 14 million cells (Mesh 2), or preferably 110 million cells (Mesh 3) to provide a certain reasonable agreement with the experimental data whereas other published LES computations of the same case, using similar codes, models, reaction mechanisms, etc., require substantially fewer cells, on the order of 5 to 10 million cells?*

A decent agreement for most of the statistics is obtained from the 14M cells mesh. However, CO profiles indeed require higher mesh resolutions due to the outer flame lift-off sensitivity. This is one of the major contribution of the paper.

*o Why are figures 10 and 11 truncated so that not all profiles are completely visible?*  
These figures are chosen to show the best the comparison to the experiment.

*o The CO profiles in figures 10 and 11 show quite modest agreement with the experimental data. Is this related to the choice of the reaction mechanism or to something else?*

In black, referees questions, comments and queries;  
 in blue, replies to referees;  
 in red, changes made to the paper.

The CO profiles are highly influenced by the kinetic scheme. The NAD3 case has been reproduced but with the BFER 2-step scheme (Franzelli et al., 2012): Fig. R1 represents the CO mass fraction compared to the experiment. It shows that the CO mass fraction is highly underestimated. A global scheme is thus unable to accurately capture the CO global behavior. A study with a more detailed kinetic scheme than the one of Sankaran is currently conducted. As shown by this article, the non-adiabatic condition impacts mostly the outer recirculation zone CO profile.

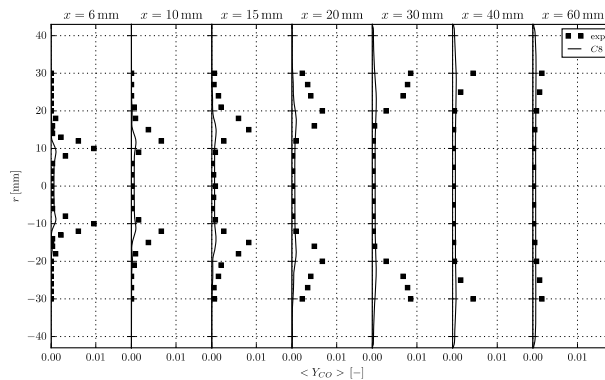


FIG R1 : CO mass fraction profile comparison to the experiment of the non-adiabatic condition with the BFER 2-step scheme and the mesh 3 (110M elements).

*o Which LES case is depicted in Fig 12?*

It has been precised in the revised version.

*o The discussion of the lift-off height and its dependence on strain and resolution is interesting but is not novel, and has been discussed previously by other investigators. Besides, it is not tied to the reaction mechanism in the way it should have been. Since no evaluation of the dependence of the reaction mechanism on the rate of strain is made here or in the original mechanism reference we simply have no idea if the results presented here are reasonable or not.*

Even if no strain influence study was conducted on 1D flame with the Sankaran kinetic scheme, the good agreement of the LES results to the experiment is a good indicator its good behavior.

# Large-Eddy Simulation of the lean-premixed PRECCINSTA burner with wall heat loss

P. Benard<sup>a,\*</sup>, G. Lartigue<sup>a</sup>, V. Moureau<sup>a</sup>, R. Mercier<sup>b</sup>

<sup>a</sup> *Normandie Univ, INSA Rouen, UNIROUEN, CNRS, CORIA, 76000 Rouen, France*

<sup>b</sup> *SAFRAN Tech, Rue des Jeunes Bois, Châteaufort - CS 80112, 78772  
Magny-les-Hameaux, France*

---

## Abstract

Swirl burners are widely used in aeronautical engines and industrial gas turbines. These burners enhance the flame stabilization by bringing back hot products to the reactive zone and their topology ensures a good compactness. However, the outer recirculation zones created in these burners induce wall heat loss that affects the flame structure. This paper proposes a numerical strategy based on Large-Eddy Simulation (LES) and non-adiabatic boundary conditions with a skeletal chemistry approach coupled to the Dynamic Thickened Flame model (TFLES). Simulations were performed on the PRECCINSTA burner with meshes up to 877 millions elements. Results demonstrated the impact of the addition of wall heat loss on the lift-off of the external flame front, leading to a flame topology change from a M-shape to a V-shape. This lift-off height increases with the grid resolution showing the strong influence of the mesh resolution on the flame topology. Comparisons of the non-adiabatic LES results on the finest mesh with the experimental data

---

\*Corresponding author

*Email address:* pierre.benard@coria.fr (P. Benard)

show an unprecedented agreement. The flame quenching process is analyzed and exhibits the role of strain rate which controls the level of penetration of cooled products within the inner reaction zone.

*Keywords:*

non-adiabatic premixed combustion, swirl burner, Large-Eddy Simulation, heat loss, skeletal chemistry

---

## 1. Introduction

Swirl-type combustion is widely used for industrial burners as it provides several advantages. When the geometrical swirl number is high enough, i.e. over 0.6, the burner exhibits a Central Recirculation Zone (CRZ) and Outer Recirculation Zones (ORZ). In these zones, hot burnt gases recirculate helping flame stabilization and extending flammability limits [1]. In premixed swirl burner, the flame structure is influenced by wall heat transfer [1]. Indeed, it has been observed that strong heat loss may influence the ORZ, weakening the stabilization process [2] up to local extinction [3].

Numerous numerical studies have been performed on the so-called PRECINSTA burner [4], a swirl lean-premixed methane-air combustor. Most of them focus on Large-Eddy Simulations (LES) with adiabatic wall conditions. These computations were not able to correctly capture the flame structure. Moureau et al. [5] and Franzelli et. al. [6, 7] agree to attribute this effect to the adiabatic wall condition or to partial premixing without being able to validate it. However, these studies demonstrated the strong influence of the mesh resolution [5] and of the chemistry description [7] on the flow and the flame topology. Indeed, Franzelli et al. [7] explained the need of ana-

lytical or skeletal schemes to accurately predict the consumption speed, the intermediate species concentration and the flame structure.

In this paper, LES of the PRECCINSTA burner are carried out with a skeletal scheme using four different grid resolutions and with adiabatic and non-adiabatic wall conditions. The objective is to study grid resolution and heat loss influence on the flame structure and pollutant formation. First, the experimental set-up and the numerical modeling are presented, as well as the strategy established to obtain the non-adiabatic condition is exposed. Then, the LES results are analyzed and compared to experimental data.

## 2. Experimental set-up

Designed within the EU project PRECCINSTA, the combustor is derived from an industrial design by SAFRAN Helicopter Engines [4, 8], representative of a real aeronautical gas turbine combustor. It was widely studied experimentally [9] or numerically [5, 6, 10–14].

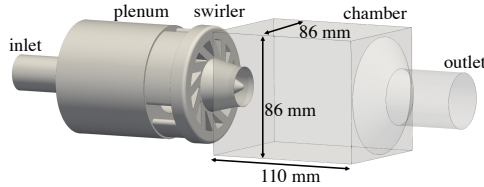


Figure 1: Computed geometry of the PRECCINSTA burner.

As described by Fig. 1, the geometry consists of three parts. The pre-mixed methane-air mixture is injected into the plenum and swirled through the injector by twelve radial veins before entering the chamber through a converging nozzle with a central conical bluff-body. The chamber has a square

Air flow rate [g/min]	734.2
Methane flow rate [g/min]	35.9
Inlet temperature [K]	300.0
Thermal power [kW]	30.0
Equivalence ratio	0.83

Table 1: Flame parameters of the experimental case.

cross-section of  $86 \times 86 \text{ mm}^2$  and a height of 110 mm. The burnt gases leave the burner by a cone-shaped exhaust pipe. 1.5 mm-thick quartz windows are placed on the combustor side walls to enable optical diagnostics. Laser Raman scattering was used to provide quantitative measurements of major species and temperature at different sections.

The present study focuses on the 30 kW “quiet” case at equivalence ratio 0.83 (see Tab. 1). Although air and methane are injected separately in the experiment, a perfectly premixed injection condition is assumed in this paper as in previous studies [5, 10, 12, 13]. At this specific operating conditions, Franzelli et al. [6] showed that this assumption has a negligible effect on the results. From Moureau et al. [5], the integral length scale is estimated as  $\ell_T = 7.0 \text{ mm}$  and the Kolmogorov length scale as  $\eta = 29 \mu\text{m}$ . The eddy turn-over time and the Precessing Vortex Core characteristic time scale have a similar value, around 2.0 ms, while the Flow Through Time is estimated around 30 ms.

### 3. Numerical modeling

Large-Eddy Simulations are performed using the in-house solver YALES2 [15]. This massively parallel finite-volume code solves the low-Mach number Navier-Stokes equations using a projection method [16] for variable density flows [17]. Density, momentum and scalar equations are solved using a 4th-order centered scheme in space and a 4th-order Runge-Kutta-like scheme in time [18]. It is able to handle unstructured meshes up to billions of elements.

Finite-rate chemistry is employed: all species appearing in the chemical mechanism plus the sensible enthalpy are transported. The source terms are evaluated from the kinetic mechanism at each control volume and for each time step. To avoid being limited by the chemical time step, an operator splitting method is used [19] relying on the stiff ODE solver CVODE [20]. A specific strategy to distribute the chemistry computation on all computing cores is adopted [21].

The kinetic scheme of Sankaran et al. [22] composed of 17 species and 73 reactions is used. This scheme is based on the GRI 1.2 mechanism [23] and dedicated to lean premixed methane-air combustion. Unstrained laminar 1D premixed flames were computed with YALES2 at the operating conditions from Tab. 1. The obtained laminar flame speed is  $s_L^0 = 0.302 \text{ m.s}^{-1}$  and thermal flame thickness is  $\delta_L^0 = 473 \mu\text{m}$ .

Turbulent sub-grid scale (SGS) stresses are modeled with the localized dynamic Smagorinsky model [24]. The kinetic scheme is coupled with the DTFLES model [25] to resolve the flame front on the LES grid and to account for SGS turbulence/chemistry interactions using the efficiency function of Charlette [26] with the fractal parameter set to  $\beta = 0.5$ .

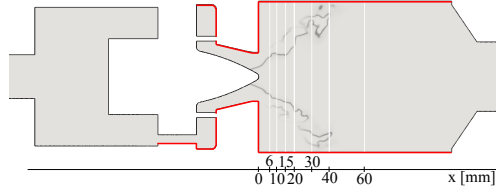


Figure 2: Adiabatic (red) and non-adiabatic (black) boundary condition for the non-adiabatic cases. Vertical white lines show the experimental temperature and species profiles.

The flame sensor, which locally activates the flame thickening is defined according to [7]. It relies on the source term of a fictive progress variable based on CO, CO<sub>2</sub> and H<sub>2</sub>O:  $\dot{\omega}_c = \dot{\omega}_{\text{CO}} + \dot{\omega}_{\text{CO}_2} + \dot{\omega}_{\text{H}_2\text{O}}$ . The flame sensor is set to 1.0 when  $\dot{\omega}_c$  exceeds 10% of its maximum value for the unstrained laminar flame, and 0.0 elsewhere. A filtering operation is performed to smooth the flame sensor away from the 10% region. This modeling strategy has been validated on 1D unstrained laminar flame and classical 2D flame-vortex interactions cases.

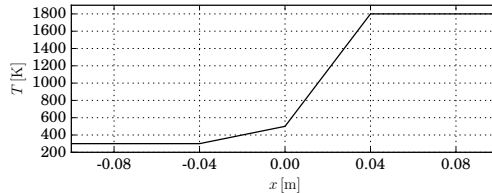


Figure 3: Wall temperature profile along the axial direction.

Convective heat transfer through the injector system and quartz windows is modeled as a local temperature Dirichlet boundary condition. The wall temperature was not measured experimentally and was obtained here

through a trial and error procedure based on non-adiabatic LES computations. The boundary condition was calibrated for mesh 2 and validated for mesh 3 (see Tab. 2). A first guess was designed from experimental data: water-cooling in the injector and natural convection for lateral walls. Then, seven temperature profiles were necessary to achieve the final results. The cost function of the optimization process was based on the temperature in the corner recirculation zones and the maximum CO mass fraction in the outer branch. It was found that almost no heat loss appear on the injector nozzle but mainly on the combustion chamber base, due to the swirler water cooling system, and quartz windows. As illustrated by Fig. 2, the nozzle is considered adiabatic, and heat transfer occurs at the external wall of the injector, the chamber base and the chamber lateral walls. The final wall temperature condition is shown in Fig. 3.

A slight preheating of the methane-air mixture was observed experimentally. This preheating is reproduced in the simulation by the heat transfer in the swirler. As a result, the temperature reaches values between 320 K and 380 K before entering the combustion chamber [8]. In this study, the preheating in the injector due to wall temperature profile induces an increase of the mean temperature to 320.5 K, which is interestingly the same as previous LES studies [6, 14], which imposed the fresh gases temperature at 320 K.

For the considered burner, LES is performed successively on meshes with 0.4, 2.3, 18.5, and 147.2 million nodes with the strategy developed in [5]. The grid size  $\Delta$  in the flame region and the ratios of the turbulence and flame length scales [5] are presented in Tab. 2.

Mesh name	1	2	3	4
#Nodes [Million]	0.4	2.3	18.5	147
#Cells [Million]	1.7	14	110	877
$\Delta$ [mm]	1.2	0.6	0.3	0.15
$\ell_T/\Delta$	5.8	11.7	23.3	46.5
$\Delta/\eta$	41.4	20.7	10.3	5.1
$\delta_L^0/\Delta$	0.35	0.71	1.41	2.83
$\langle \max(\mathcal{F}) \rangle$	16.6	10.3	5.7	3.3

Table 2: Resolution parameters for the LES computational grids.

#### 4. Results and discussion

All the performed LES computations are listed in Tab. 3, combining the different meshes and wall thermal conditions. As shown in Tab. 2, the time-averaged maximum value of the thickening factor  $\mathcal{F}$  decreases at each grid refinement. However, even with the most refined mesh composed of 877 million elements, the SGS flame-turbulence interaction model is still necessary but is expected to have a very small impact on the results. A maximum thickening of around 3 means that the equivalent laminar non-thickened flame is resolved with a grid spacing of  $50 \mu\text{m}$ . At this resolution, the relative error on the laminar flame speed is less than 0.5% and species profiles are correctly reproduced.

The non-adiabatic cases present different wall heat loss amplitude as revealed by Tab. 3. The integral of the heat flux on the walls for the NAD2, NAD3 and NAD4 cases show a similar amplitude, around 1800 W, while it

Case name	AD1	NAD1	AD2	NAD2	AD3	NAD3	NAD4
Mesh	1	1	2	2	3	3	4
Thermal condition	AD	NAD	AD	NAD	AD	NAD	NAD
External flame lift-off height [mm]	-	1.9	-	3.3	-	5.3	25.7
Time-averaged heat losses [kW]	-	0.99	-	1.81	-	1.91	1.78
Physical time [ms]	34.9	47.6	83.9	83.6	51.7	51.3	33.4
CPU time [ $\times 10^5$ hCPU]	0.015	0.022	0.24	0.24	3.1	3.6	36.9

Table 3: Summary of all the LES cases. AD refers to adiabatic wall condition and NAD to non-adiabatic wall condition.

is underestimated of 80% for the NAD1 case, due to the poor resolution.

The flame structure is illustrated in Fig. 4 via an iso-contour of the normalized progress variable  $c = 0.7$  where the heat release rate exceeds 1% of its maximum value. With the coarsest mesh and adiabatic condition, the flame surface does not exhibit resolved wrinkling. As the resolution increases, resolved wrinkling appears and pockets of reactants detach from the flame front. The flame presents an M-shape structure with an internal flame attached to the nozzle and an external front attached to the chamber base.

Figure 5a compares the time-averaged temperature profiles obtained on all meshes to the experiment at seven sections in the combustion chamber. The LES computations AD2 and AD3 correctly reproduce the CRZ and the flame front, while the AD1 case underestimates the temperature in the CRZ due to the large thickening of the flame. The ORZ temperature is overestimated in all cases since wall heat loss is missing. On the RMS temperature profiles of Fig. 5b, the AD1 case exhibits very low dynamics. On the con-

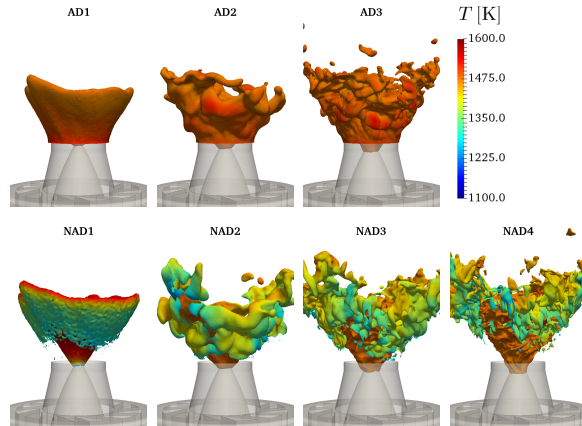


Figure 4: Normalized progress variable iso-contour  $c = 0.7$ , conditioned to heat release rate values exceeding 1% of its maximum value, colored by the temperature.

trary, even if the AD2 and AD3 cases underestimate the fluctuations in the ORZ compared to the experimental data, they provide a good agreement elsewhere.

The comparison of time-averaged and RMS carbon dioxide ( $\text{CO}_2$ ) mass fraction profiles to the experiment in Fig. 7a and Fig. 7b reveals that the adiabatic condition is in good agreement with experiment. Only the RMS profiles of the AD1 case are far from the experimental data as for the temperature, due to lack of dynamics.

As illustrated by Fig. 4, when heat loss occurs, the temperature in the reaction zone ( $c = 0.7$ ) of the outer flame front lies between 1300 and 1500 K while 1550 K is found in the adiabatic cases. This is confirmed by the mean temperature profiles of Fig. 6a showing that, in addition to the CRZ and flame front area, the ORZ is well captured with a mean temperature around 1800 K at the first section  $x = 6$  mm, i.e. 200 K less than the adiabatic cases.

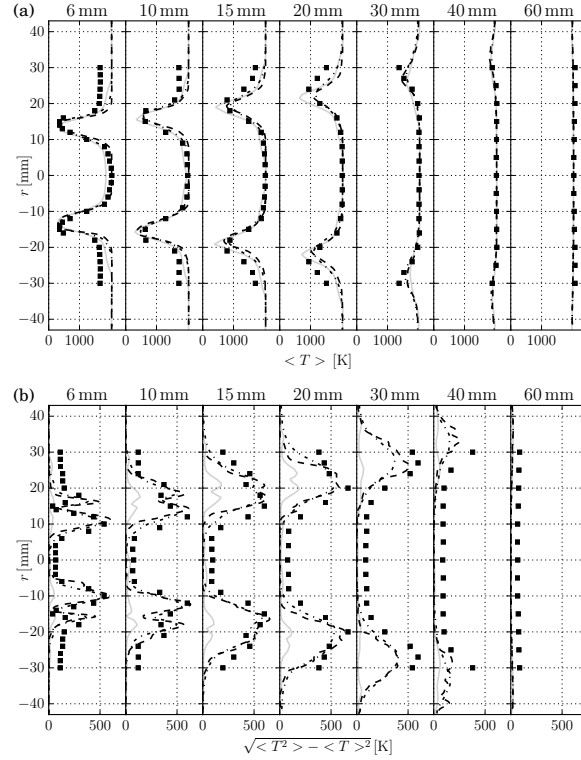


Figure 5: Mean (a) and RMS (b) temperature profiles for AD1 (—), AD2 (-·-·), AD3 (- - -) cases and experiment (■).

The same trend is observed on RMS profiles of Fig. 6b: the fluctuations are correctly captured everywhere except for the NAD1 case. The addition of heat loss has a negligible effect on mean  $\text{CO}_2$  mass fraction profiles as shown by Fig. 8a. The RMS profiles of Fig. 8b indicate a slightly better prediction of  $Y_{\text{CO}_2}$  fluctuations in the ORZ part, compared to adiabatic cases.

The flame structure changes with the thermal wall condition. Figure 4 shows a detached external flame front in the non-adiabatic cases. The lift-off height was measured based on the time-averaged flame sensor, which is

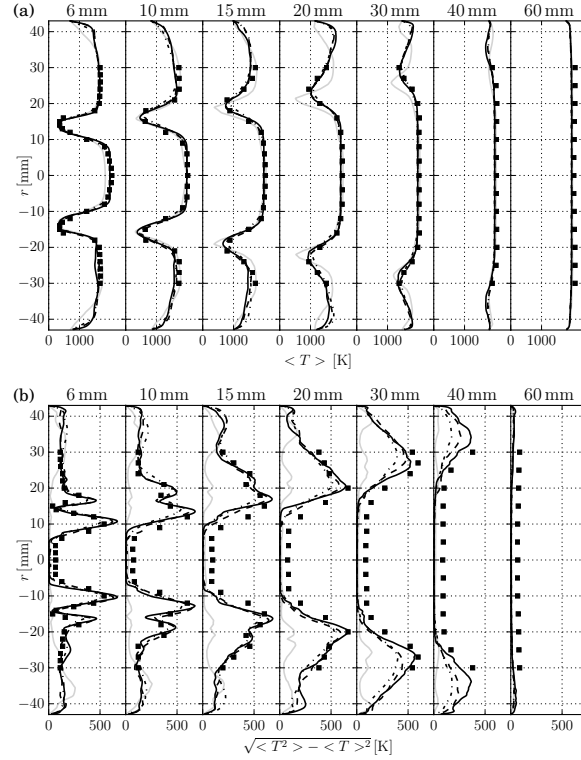


Figure 6: Mean (a) and RMS (b) temperature profiles for NAD1 (—), NAD2 (-·-·), NAD3 (- - -), NAD4 (—) cases and experiment (■).

linked to the local maximum of heat release, and collected in Tab. 3. With the increase of the mesh resolution, the lift-off height (LOH) grows up from 1.9 to 25.7 mm, leading to a V-shape flame for NAD4.

This V-shape flame structure is observed experimentally as confirmed by the CO profiles shown in Figs. 9a and 10a. The adiabatic cases exhibit a double  $Y_{\text{CO}}$  peak on the first sections whatever the resolution, representative of a double flame front. Contrarily to the results of Franzelli et al. [6] in the same operating conditions, the use of a skeletal kinetic scheme here allows to

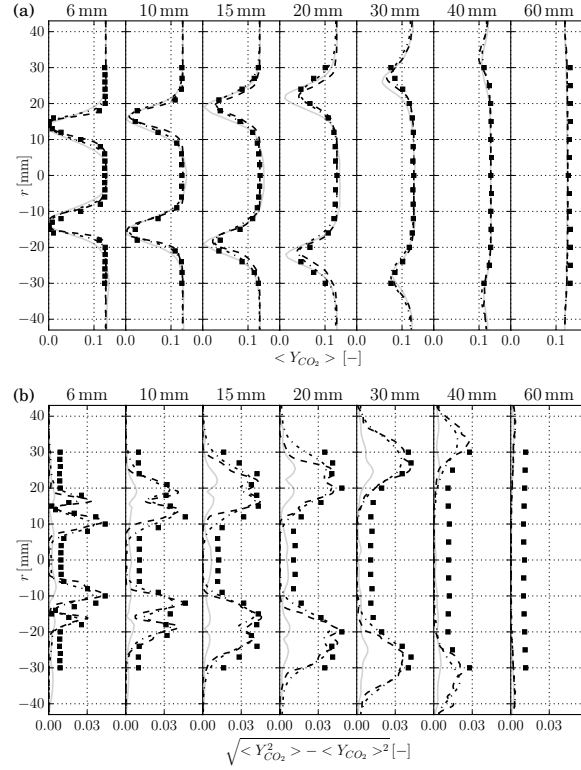


Figure 7: Mean (a) and RMS (b)  $\text{CO}_2$  mass fraction profiles for AD1 (—), AD2 (-.-.), AD3 (- - -) cases and experiment (■).

capture the CO behavior. The addition of heat loss enables to annihilate the external flame front. The NAD4 case reproduces very well the experimental  $Y_{\text{CO}}$  profiles: only a slight overestimation is found in the ORZ. As the cell size increases, the  $Y_{\text{CO}}$  profiles increase globally. This is due to a known behavior of the TFLES turbulent combustion model: as the flame is thickened, the integral of intermediate species profile is artificially increased [27].

The  $Y_{\text{CO}}$  RMS profiles are plotted in Figs. 9b and 10b for the adiabatic and the non-adiabatic cases, respectively. In the adiabatic cases, except AD1,

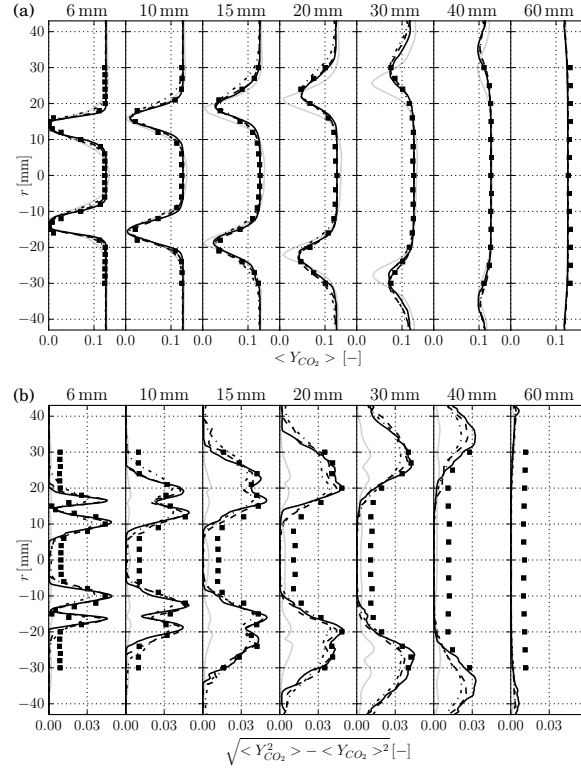


Figure 8: Mean (a) and RMS (b) CO<sub>2</sub> mass fraction profiles for NAD1 (—), NAD2 (-·-·), NAD3 (- - -), NAD4 (—) cases and experiment (■).

the experiment profiles are retrieved only for the inner flame. The dynamics in the non-adiabatic cases is well reproduced with less fluctuations for the outer flame front. NAD4 shows the best agreement to the experiment.

Figure 11 compares the OH-LIF measurements to instantaneous OH concentrations on AD3, NAD3 and NAD4 cases. It is observed that the intermediate species OH is produced in the reaction zone and almost entirely destroyed in the post-flame area. In the non-adiabatic case, no gradient of the OH mass fraction is found in the ORZ as in the experiment. Moreover,

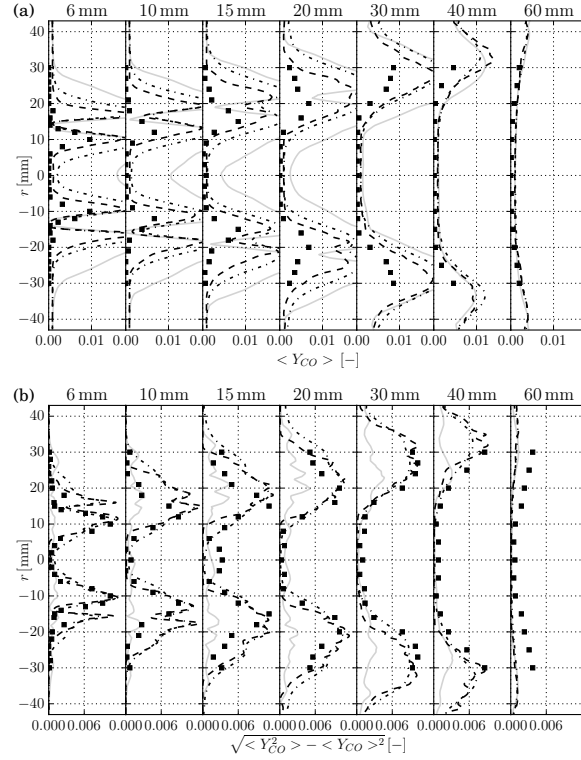


Figure 9: Mean (a) and RMS (b) CO mass fraction profiles for AD1 (—), AD2 (-·-·), AD3 (- - -) cases and experiment (■).

the NAD4 case seems to have the best agreement in terms of flame wrinkling and spatial distribution of OH mass fraction gradient compared to the experiment.

The outer flame front extinction is now analyzed by introducing the local enthalpy defect  $\Delta H = H - H_{\text{ad}}$  where  $H$  and  $H_{\text{ad}}$  are the local total enthalpy and the total enthalpy of the adiabatic mixture, respectively. A 2-D longitudinal cut of the NAD4 case colored by the instantaneous value of  $\Delta H$  is shown in Fig. 12 and confirms that the slow characteristic time

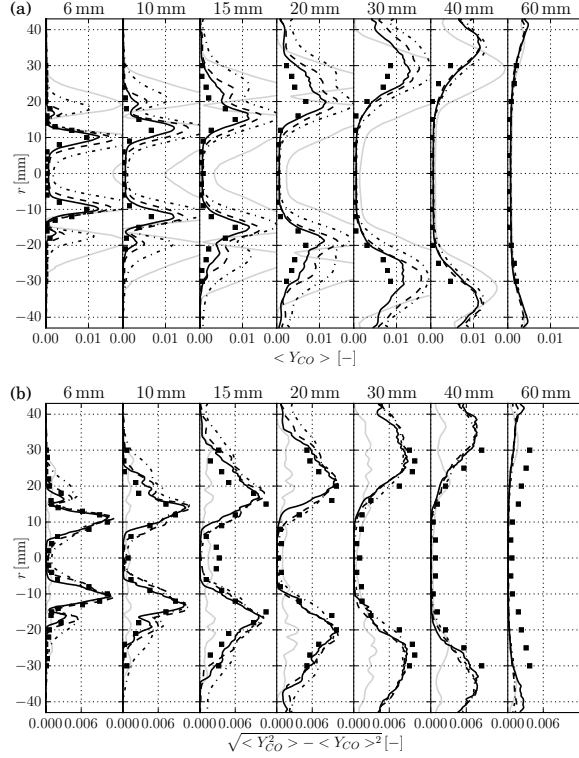


Figure 10: Mean (a) and RMS (b) CO mass fraction profiles for NAD1 (—), NAD2 (— · —), NAD3 (---), NAD4 (— —) cases and experiment (■).

scale of the ORZ promotes heat exchange at the burner walls and causes a drastic fall of total enthalpy in this region. The impact of the enthalpy defect on the outer flame structure is analyzed in Fig. 13 by plotting, for the NAD4 case, a scatter-plot of the heat release rate  $\dot{\omega}_T/\mathcal{F}$  conditioned to  $c \in [0.75 - 0.8]$  against the velocity gradient norm  $|\nabla \mathbf{u}|$ . The velocity gradient is used here as an indicator of the local strain rate seen by the flame front and each point is colored by its local enthalpy defect. Red points corresponds to adiabatic zones while the level of heat loss increases for colors

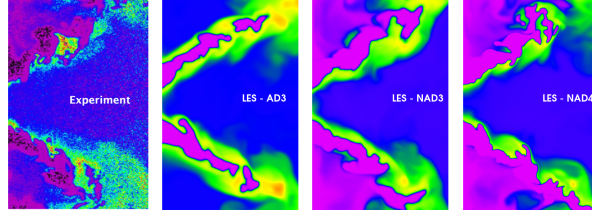


Figure 11: Comparison of OH – LIF measurements to instantaneous OH normalized concentration from LES cases. From left to right: experiment, AD3, NAD3 and NAD4 cases. Colormap: 0.0 0.25 0.5 0.75 1.0.

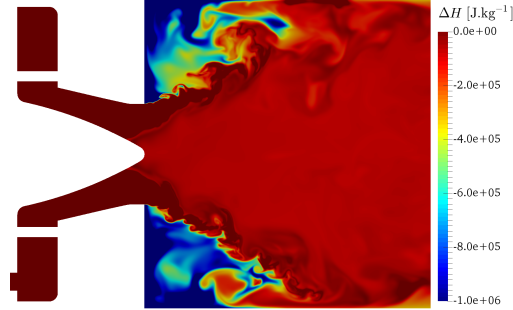


Figure 12: Instantaneous enthalpy defect on the mid-plane for NAD4.

reaching dark blue. Three main zones can be identified: (i) A high density of red points (adiabatic) is located at high heat release rates ( $\dot{\omega}_T/\mathcal{F} > 2.10^9$  W.m<sup>3</sup>): they mainly belong to the internal flame front which remains adiabatic and correspond to  $|\nabla\mathbf{u}| \in [10000; 15000]$  s<sup>-1</sup>; (ii) A low density of blue points (high enthalpy defect) is located at moderate heat release rates ( $\dot{\omega}_T/\mathcal{F} \in [1.10^9; 2.10^9]$  W.m<sup>3</sup>): they correspond to the reactive outer flame front which is subjected to heat loss and a similar velocity gradient as the inner flame front; (iii) A high density of blue points (high enthalpy defect) is located at the bottom of the figure ( $\dot{\omega}_T \approx 0$ ) and corresponds to higher

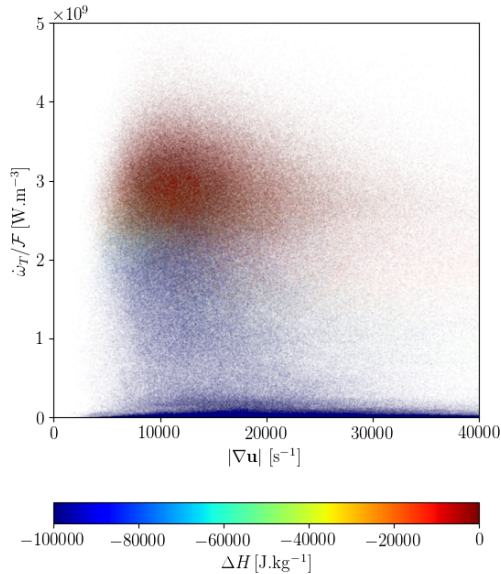


Figure 13: Scatter plot of the heat release rate against the velocity gradient norm, for points with  $c \in [0.75 - 0.8]$ , colored by the enthalpy defect for NAD4 simulation.

values of  $|\nabla\mathbf{u}| \in [10000; 40000]$  s<sup>-1</sup>: they correspond to the quenched outer branch where mixing between adiabatic fresh gases and cooled burnt gases occurs without chemical activity. Interestingly, for the same levels of  $\Delta H$  and  $c$ , (ii) and (iii) exhibit both reacting and quenched flame fronts suggesting that enthalpy defect is not the only physical phenomenon controlling the flame quenching process. However, considering both strain rate (estimated here through  $|\nabla\mathbf{u}|$ ) and enthalpy defect  $\Delta H$  allows to clearly discriminate the reacting points with low strain rates (ii) and quenched points with higher strain rates (iii). The increase of the LOH shown in Tab. 3 is therefore due to higher resolved strain rates on the refined grids leading to an increase of the quenched flame surface. This conclusion is in line with previous studies

performed on counterflow flame configurations [28] showing that burnt gases enthalpy defect decreases the resistance of premixed flame fronts to large strain rates.

## 5. Conclusions

In this work, a numerical strategy to take into account wall heat loss on the lean premixed methane-air PRECCINSTA burner has been proposed. This methodology relies on high-fidelity LES, a skeletal kinetic scheme, the DTFLES model and a wall temperature Dirichlet boundary condition. The results were compared to adiabatic computations and to experimental data. Different grid resolutions were tested, with meshes containing from 1.7 up to 877 millions of elements. The results show that the flame structure is strongly affected by the wall heat transfer whatever the grid size. The enthalpy defect in burnt gases enhances the sensitivity to local strain rate leading to quenching of the outer flame front and changing the flame topology to a V-shape. The temperature and CO distributions are then highly affected. The non-adiabatic case with the most refined grid shows the best agreement to experimental results. Indeed, the V-shape flame structure, the front wrinkling, the temperature and species profiles as well as OH distribution are recovered, confirming the importance of taking into account wall heat loss and complex chemistry effects in such configuration. **These results may further be used to develop a sub-grid model closure able to accurately capture intermediate species.**

## Acknowledgments

This work was granted access to the HPC resources from CINES under the allocations A0032B06880 made by GENCI and from CRIANN under the allocation 2012006.

## References

- [1] T. Poinsot, D. Veynante, Theoretical and numerical combustion, RT Edwards, Inc., 2005.
- [2] N. Syred, J. Beer, *Combust. Flame* 23 (2) (1974) 143–201.
- [3] R. Mercier, P. Auzillon, V. Moureau, N. Darabiha, O. Gicquel, D. Veynante, B. Fiorina, *Flow, Turbul. Combust.* 93 (2014) 349–381
- [4] G. Lartigue, U. Meier, C. Berat, *Appl. Therm. Eng.* 24 (11) (2004) 1583–1592.
- [5] V. Moureau, P. Domingo, L. Vervisch, *Combust. Flame* 158 (7) (2010) 1340–1357.
- [6] B. Franzelli, E. Riber, L. Y. M. Gicquel, T. Poinsot, *Combust. Flame* 159 (2) (2012) 621–637.
- [7] B. Franzelli, E. Riber, B. Cuenot, *C. R. Mec.* 341 (1-2) (2013) 247–256.
- [8] W. Meier, P. Weigand, X. R. Duan, R. Giezendanner-Thoben, *Combust. Flame* 150 (1-2) (2007) 2–26.
- [9] P. Weigand, X. R. Duan, W. Meier, U. Meier, M. Aigner, C. Brat, *Proc. of the European Combustion Meeting*, 2005, p. 235.

- [10] S. Roux, G. Lartigue, T. Poinsot, U. Meier, C. Brat, *Combust. Flame* 141 (1-2) (2005) 40–54.
- [11] V. Moureau, P. Minot, H. Pitsch, C. Brat, *J. Comput. Phys.* 221 (2) (2007) 600–614.
- [12] B. Fiorina, R. Vicquelin, P. Auzillon, N. Darabiha, O. Gicquel, D. Veynante, *Combust. Flame* 157 (2010) 465–475.
- [13] P. Wang, J. Frhlich, U. Maas, Z. Hea, C. Wang, *Combust. Flame* 164 (2016) 329–345.
- [14] J. M. Lourier, M. Sto hr, B. Noll, S. Werner, A. Fiolitakis, *Combust. Flame* 183 (2017) 343–357.
- [15] V. Moureau, P. Domingo, L. Vervisch, *C. R. Mec.* 339(2/3) (2-3) (2011) 141–148.
- [16] A.J. Chorin, *Math. Comp.* 22 (1968) 745–762.
- [17] C. D. Pierce, P. Moin, *J. Fluid Mech.* 504 (2004) 73–97.
- [18] M.Kraushaar, Ph.D.thesis, CERFACS (2011).
- [19] R. Yu, J. Yu, X.-S. Bai, *J. Comput. Phys.* 231 (16) (2012) 5504–5521.
- [20] S. D. Cohen, A. C. Hindmarsh, *Comput. Phys.* 10 (2) (1996) 138–143.
- [21] P. Benard, V. Moureau, G. Lartigue, Y. DAngelo, *Int. J. Hydrogen Energy* 42 (4) (2017) 2397–2410.

- [22] R. Sankaran, E.R. Hawkes, J.H. Chen, T. Lu, C.K. Law, *Proc. Combust. Inst.* 31 (2007) 1291–1298.
- [23] G. Smith, D. Golden, M. Frenklach, N. Moriarty, B. Eiteneer, M. Goldenberg, C. Bowman, R. Hanson, S. Song, W. Gardiner, et al., *Technical Report*, Gas Research Institute (1999).
- [24] M. Germano, U. Piomelli, P. Moin, W. H. Cabot, *Phys. Fluids A* 3 (7) (1991) 1760–1765.
- [25] O. Colin, F. Ducros, D. Veynante, T. Poinso, *Phys. Fluids* 12 (7) (2000) 1843–1863.
- [26] F. Charlette, C. Meneveau, D. Veynante, *Combust. Flame* 131 (2002) 181–197.
- [27] M. Cailler, R. Mercier, V. Moureau, N. Darabiha, B. Fiorina, 55th AIAA Aerospace Sciences Meeting, AIAA 2017-0606 (2017).
- [28] B. Coriton, M.D. Smooke, A. Gomez, *Combust. Flame* 157 (11) (2010) 2155–2164

# Large-Eddy Simulation of the lean-premixed PRECCINSTA burner with wall heat loss

P. Benard<sup>a,\*</sup>, G. Lartigue<sup>a</sup>, V. Moureau<sup>a</sup>, R. Mercier<sup>b</sup>

<sup>a</sup> *Normandie Univ, INSA Rouen, UNIROUEN, CNRS, CORIA, 76000 Rouen, France*

<sup>b</sup> *SAFRAN Tech, Rue des Jeunes Bois, Châteaufort - CS 80112, 78772  
Magny-les-Hameaux, France*

---

## Abstract

Swirl burners are widely used in aeronautical engines and industrial gas turbines. These burners enhance the flame stabilization by bringing back hot products to the reactive zone and their topology ensures a good compactness. However, the outer recirculation zones created in these burners induce wall heat loss that affects the flame structure. This paper proposes a numerical strategy based on Large-Eddy Simulation (LES) and non-adiabatic boundary conditions with a skeletal chemistry approach coupled to the Dynamic Thickened Flame model (TFLES). Simulations were performed on the PRECCINSTA burner with meshes up to 877 millions elements. Results demonstrated the impact of the addition of wall heat loss on the lift-off of the external flame front, leading to a flame topology change from a M-shape to a V-shape. This lift-off height increases with the grid resolution showing the strong influence of the mesh resolution on the flame topology. Comparisons of the non-adiabatic LES results on the finest mesh with the experimental data

---

\*Corresponding author

*Email address:* pierre.benard@coria.fr (P. Benard)

show an unprecedented agreement. The flame quenching process is analyzed and exhibits the role of strain rate which controls the level of penetration of cooled products within the inner reaction zone.

*Keywords:*

non-adiabatic premixed combustion, swirl burner, Large-Eddy Simulation, heat loss, skeletal chemistry

---

## 1. Introduction

Swirl-type combustion is widely used for industrial burners as it provides several advantages. When the geometrical swirl number is high enough, i.e. over 0.6, the burner exhibits a Central Recirculation Zone (CRZ) and Outer Recirculation Zones (ORZ). In these zones, hot burnt gases recirculate helping flame stabilization and extending flammability limits [1]. In premixed swirl burner, the flame structure is influenced by wall heat transfer [1]. Indeed, it has been observed that strong heat loss may influence the ORZ, weakening the stabilization process [2] up to local extinction [3].

Numerous numerical studies have been performed on the so-called PRECINSTA burner [4], a swirl lean-premixed methane-air combustor. Most of them focus on Large-Eddy Simulations (LES) with adiabatic wall conditions. These computations were not able to correctly capture the flame structure. Moureau et al. [5] and Franzelli et. al. [6, 7] agree to attribute this effect to the adiabatic wall condition or to partial premixing without being able to validate it. However, these studies demonstrated the strong influence of the mesh resolution [5] and of the chemistry description [7] on the flow and the flame topology. Indeed, Franzelli et al. [7] explained the need of ana-

lytical or skeletal schemes to accurately predict the consumption speed, the intermediate species concentration and the flame structure.

In this paper, LES of the PRECCINSTA burner are carried out with a skeletal scheme using four different grid resolutions and with adiabatic and non-adiabatic wall conditions. The objective is to study grid resolution and heat loss influence on the flame structure and pollutant formation. First, the experimental set-up and the numerical modeling are presented, as well as the strategy established to obtain the non-adiabatic condition is exposed. Then, the LES results are analyzed and compared to experimental data.

## 2. Experimental set-up

Designed within the EU project PRECCINSTA, the combustor is derived from an industrial design by SAFRAN Helicopter Engines [4, 8], representative of a real aeronautical gas turbine combustor. It was widely studied experimentally [9] or numerically [5, 6, 10–14].

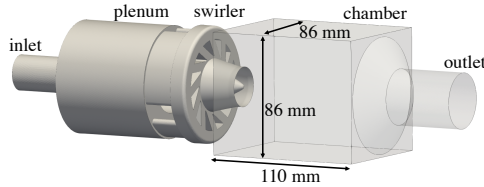


Figure 1: Computed geometry of the PRECCINSTA burner.

As described by Fig. 1, the geometry consists of three parts. The pre-mixed methane-air mixture is injected into the plenum and swirled through the injector by twelve radial veins before entering the chamber through a converging nozzle with a central conical bluff-body. The chamber has a square

Air flow rate [g/min]	734.2
Methane flow rate [g/min]	35.9
Inlet temperature [K]	300.0
Thermal power [kW]	30.0
Equivalence ratio	0.83

Table 1: Flame parameters of the experimental case.

cross-section of  $86 \times 86 \text{ mm}^2$  and a height of 110 mm. The burnt gases leave the burner by a cone-shaped exhaust pipe. 1.5 mm-thick quartz windows are placed on the combustor side walls to enable optical diagnostics. Laser Raman scattering was used to provide quantitative measurements of major species and temperature at different sections.

The present study focuses on the 30 kW “quiet” case at equivalence ratio 0.83 (see Tab. 1). Although air and methane are injected separately in the experiment, a perfectly premixed injection condition is assumed in this paper as in previous studies [5, 10, 12, 13]. At this specific operating conditions, Franzelli et al. [6] showed that this assumption has a negligible effect on the results. From Moureau et al. [5], the integral length scale is estimated as  $\ell_T = 7.0 \text{ mm}$  and the Kolmogorov length scale as  $\eta = 29 \mu\text{m}$ . The eddy turn-over time and the Precessing Vortex Core characteristic time scale have a similar value, around 2.0 ms, while the Flow Through Time is estimated around 30 ms.

### 3. Numerical modeling

Large-Eddy Simulations are performed using the in-house solver YALES2 [15]. This massively parallel finite-volume code solves the low-Mach number Navier-Stokes equations using a projection method [16] for variable density flows [17]. Density, momentum and scalar equations are solved using a 4th-order centered scheme in space and a 4th-order Runge-Kutta-like scheme in time [18]. It is able to handle unstructured meshes up to billions of elements.

Finite-rate chemistry is employed: all species appearing in the chemical mechanism plus the sensible enthalpy are transported. The source terms are evaluated from the kinetic mechanism at each control volume and for each time step. To avoid being limited by the chemical time step, an operator splitting method is used [19] relying on the stiff ODE solver CVODE [20]. A specific strategy to distribute the chemistry computation on all computing cores is adopted [21].

The kinetic scheme of Sankaran et al. [22] composed of 17 species and 73 reactions is used. This scheme is based on the GRI 1.2 mechanism [23] and dedicated to lean premixed methane-air combustion. Unstrained laminar 1D premixed flames were computed with YALES2 at the operating conditions from Tab. 1. The obtained laminar flame speed is  $s_L^0 = 0.302 \text{ m.s}^{-1}$  and thermal flame thickness is  $\delta_L^0 = 473 \mu\text{m}$ .

Turbulent sub-grid scale (SGS) stresses are modeled with the localized dynamic Smagorinsky model [24]. The kinetic scheme is coupled with the DTFLES model [25] to resolve the flame front on the LES grid and to account for SGS turbulence/chemistry interactions using the efficiency function of Charlette [26] with the fractal parameter set to  $\beta = 0.5$ .

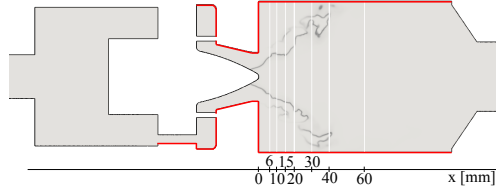


Figure 2: Adiabatic (red) and non-adiabatic (black) boundary condition for the non-adiabatic cases. Vertical white lines show the experimental temperature and species profiles.

The flame sensor, which locally activates the flame thickening is defined according to [7]. It relies on the source term of a fictive progress variable based on CO, CO<sub>2</sub> and H<sub>2</sub>O:  $\dot{\omega}_c = \dot{\omega}_{\text{CO}} + \dot{\omega}_{\text{CO}_2} + \dot{\omega}_{\text{H}_2\text{O}}$ . The flame sensor is set to 1.0 when  $\dot{\omega}_c$  exceeds 10% of its maximum value for the unstrained laminar flame, and 0.0 elsewhere. A filtering operation is performed to smooth the flame sensor away from the 10% region. This modeling strategy has been validated on 1D unstrained laminar flame and classical 2D flame-vortex interactions cases.

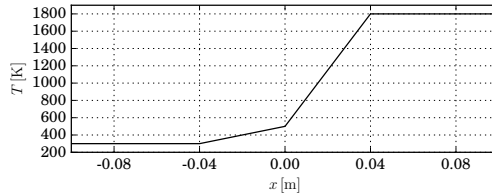


Figure 3: Wall temperature profile along the axial direction.

Convective heat transfer through the injector system and quartz windows is modeled as a local temperature Dirichlet boundary condition. The wall temperature was not measured experimentally and was obtained here

through a trial and error procedure based on non-adiabatic LES computations. The boundary condition was calibrated for mesh 2 and validated for mesh 3 (see Tab. 2). A first guess was designed from experimental data: water-cooling in the injector and natural convection for lateral walls. Then, seven temperature profiles were necessary to achieve the final results. The cost function of the optimization process was based on the temperature in the corner recirculation zones and the maximum CO mass fraction in the outer branch. It was found that almost no heat loss appear on the injector nozzle but mainly on the combustion chamber base, due to the swirler water cooling system, and quartz windows. As illustrated by Fig. 2, the nozzle is considered adiabatic, and heat transfer occurs at the external wall of the injector, the chamber base and the chamber lateral walls. The final wall temperature condition is shown in Fig. 3.

A slight preheating of the methane-air mixture was observed experimentally. This preheating is reproduced in the simulation by the heat transfer in the swirler. As a result, the temperature reaches values between 320 K and 380 K before entering the combustion chamber [8]. In this study, the preheating in the injector due to wall temperature profile induces an increase of the mean temperature to 320.5 K, which is interestingly the same as previous LES studies [6, 14], which imposed the fresh gases temperature at 320 K.

For the considered burner, LES is performed successively on meshes with 0.4, 2.3, 18.5, and 147.2 million nodes with the strategy developed in [5]. The grid size  $\Delta$  in the flame region and the ratios of the turbulence and flame length scales [5] are presented in Tab. 2.

Mesh name	1	2	3	4
#Nodes [Million]	0.4	2.3	18.5	147
#Cells [Million]	1.7	14	110	877
$\Delta$ [mm]	1.2	0.6	0.3	0.15
$\ell_T/\Delta$	5.8	11.7	23.3	46.5
$\Delta/\eta$	41.4	20.7	10.3	5.1
$\delta_L^0/\Delta$	0.35	0.71	1.41	2.83
$\langle \max(\mathcal{F}) \rangle$	16.6	10.3	5.7	3.3

Table 2: Resolution parameters for the LES computational grids.

#### 4. Results and discussion

All the performed LES computations are listed in Tab. 3, combining the different meshes and wall thermal conditions. As shown in Tab. 2, the time-averaged maximum value of the thickening factor  $\mathcal{F}$  decreases at each grid refinement. However, even with the most refined mesh composed of 877 million elements, the SGS flame-turbulence interaction model is still necessary but is expected to have a very small impact on the results. A maximum thickening of around 3 means that the equivalent laminar non-thickened flame is resolved with a grid spacing of  $50 \mu\text{m}$ . At this resolution, the relative error on the laminar flame speed is less than 0.5% and species profiles are correctly reproduced.

The non-adiabatic cases present different wall heat loss amplitude as revealed by Tab. 3. The integral of the heat flux on the walls for the NAD2, NAD3 and NAD4 cases show a similar amplitude, around 1800 W, while it

Case name	AD1	NAD1	AD2	NAD2	AD3	NAD3	NAD4
Mesh	1	1	2	2	3	3	4
Thermal condition	AD	NAD	AD	NAD	AD	NAD	NAD
External flame lift-off height [mm]	-	1.9	-	3.3	-	5.3	25.7
Time-averaged heat losses [kW]	-	0.99	-	1.81	-	1.91	1.78
Physical time [ms]	34.9	47.6	83.9	83.6	51.7	51.3	33.4
CPU time [ $\times 10^5$ hCPU]	0.015	0.022	0.24	0.24	3.1	3.6	36.9

Table 3: Summary of all the LES cases. AD refers to adiabatic wall condition and NAD to non-adiabatic wall condition.

is underestimated of 80% for the NAD1 case, due to the poor resolution.

The flame structure is illustrated in Fig. 4 via an iso-contour of the normalized progress variable  $c = 0.7$  where the heat release rate exceeds 1% of its maximum value. With the coarsest mesh and adiabatic condition, the flame surface does not exhibit resolved wrinkling. As the resolution increases, resolved wrinkling appears and pockets of reactants detach from the flame front. The flame presents an M-shape structure with an internal flame attached to the nozzle and an external front attached to the chamber base.

Figure 5a compares the time-averaged temperature profiles obtained on all meshes to the experiment at seven sections in the combustion chamber. The LES computations AD2 and AD3 correctly reproduce the CRZ and the flame front, while the AD1 case underestimates the temperature in the CRZ due to the large thickening of the flame. The ORZ temperature is overestimated in all cases since wall heat loss is missing. On the RMS temperature profiles of Fig. 5b, the AD1 case exhibits very low dynamics. On the con-

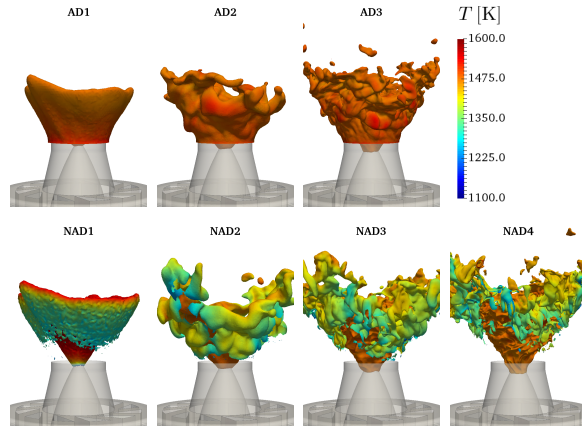


Figure 4: Normalized progress variable iso-contour  $c = 0.7$ , conditioned to heat release rate values exceeding 1% of its maximum value, colored by the temperature.

trary, even if the AD2 and AD3 cases underestimate the fluctuations in the ORZ compared to the experimental data, they provide a good agreement elsewhere.

The comparison of time-averaged and RMS carbon dioxide ( $\text{CO}_2$ ) mass fraction profiles to the experiment in Fig. 7a and Fig. 7b reveals that the adiabatic condition is in good agreement with experiment. Only the RMS profiles of the AD1 case are far from the experimental data as for the temperature, due to lack of dynamics.

As illustrated by Fig. 4, when heat loss occurs, the temperature in the reaction zone ( $c = 0.7$ ) of the outer flame front lies between 1300 and 1500 K while 1550 K is found in the adiabatic cases. This is confirmed by the mean temperature profiles of Fig. 6a showing that, in addition to the CRZ and flame front area, the ORZ is well captured with a mean temperature around 1800 K at the first section  $x = 6$  mm, i.e. 200 K less than the adiabatic cases.

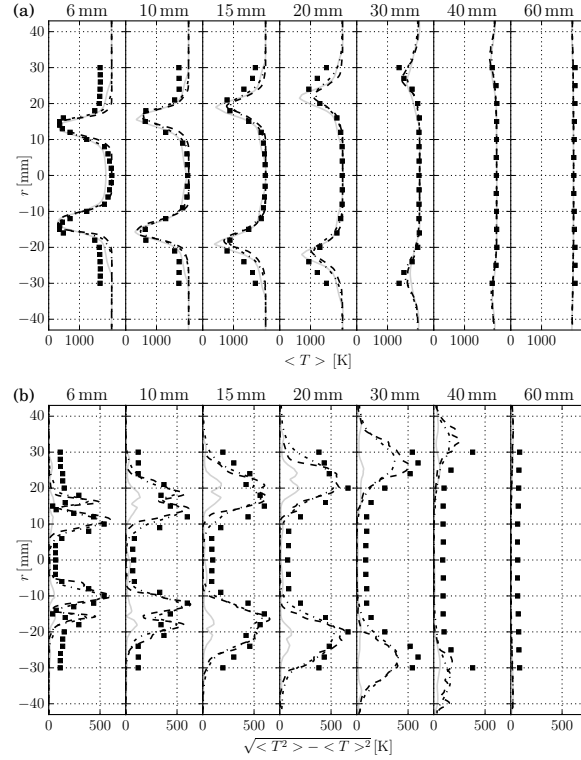


Figure 5: Mean (a) and RMS (b) temperature profiles for AD1 (—), AD2 (-·-·), AD3 (- - -) cases and experiment (■).

The same trend is observed on RMS profiles of Fig. 6b: the fluctuations are correctly captured everywhere except for the NAD1 case. The addition of heat loss has a negligible effect on mean  $\text{CO}_2$  mass fraction profiles as shown by Fig. 8a. The RMS profiles of Fig. 8b indicate a slightly better prediction of  $Y_{\text{CO}_2}$  fluctuations in the ORZ part, compared to adiabatic cases.

The flame structure changes with the thermal wall condition. Figure 4 shows a detached external flame front in the non-adiabatic cases. The lift-off height was measured based on the time-averaged flame sensor, which is

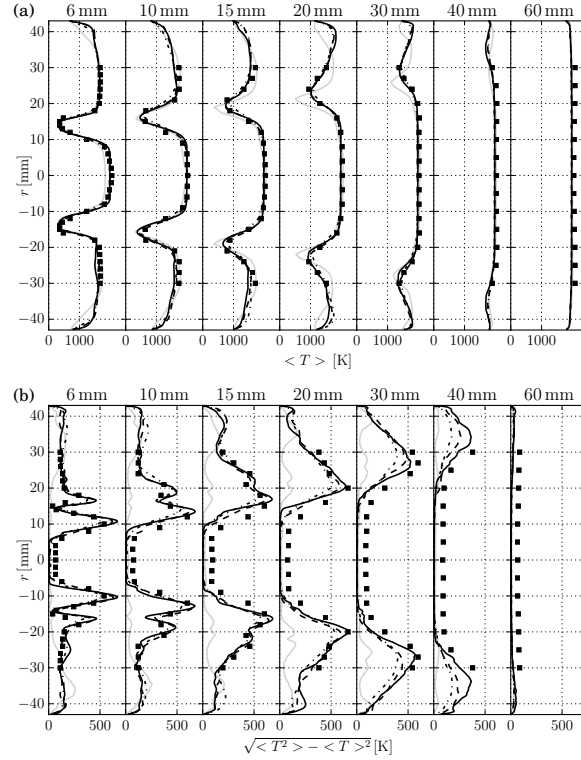


Figure 6: Mean (a) and RMS (b) temperature profiles for NAD1 (—), NAD2 (-·-·), NAD3 (·-·-), NAD4 (—) cases and experiment (■).

linked to the local maximum of heat release, and collected in Tab. 3. With the increase of the mesh resolution, the lift-off height (LOH) grows up from 1.9 to 25.7 mm, leading to a V-shape flame for NAD4.

This V-shape flame structure is observed experimentally as confirmed by the CO profiles shown in Figs. 9a and 10a. The adiabatic cases exhibit a double  $Y_{\text{CO}}$  peak on the first sections whatever the resolution, representative of a double flame front. Contrarily to the results of Franzelli et al. [6] in the same operating conditions, the use of a skeletal kinetic scheme here allows to

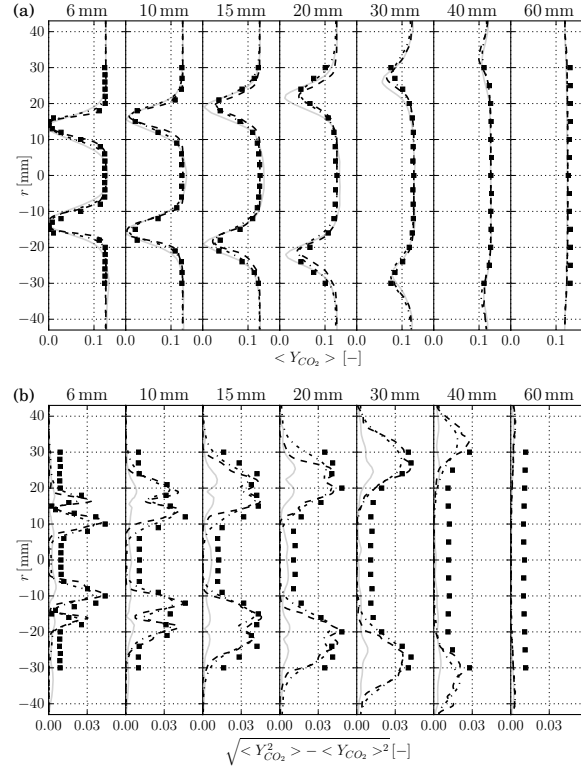


Figure 7: Mean (a) and RMS (b) CO<sub>2</sub> mass fraction profiles for AD1 (—), AD2 (-.-.), AD3 (- - -) cases and experiment (■).

capture the CO behavior. The addition of heat loss enables to annihilate the external flame front. The NAD4 case reproduces very well the experimental  $Y_{CO}$  profiles: only a slight overestimation is found in the ORZ. As the cell size increases, the  $Y_{CO}$  profiles increase globally. This is due to a known behavior of the TFLES turbulent combustion model: as the flame is thickened, the integral of intermediate species profile is artificially increased [27].

The  $Y_{CO}$  RMS profiles are plotted in Figs. 9b and 10b for the adiabatic and the non-adiabatic cases, respectively. In the adiabatic cases, except AD1,

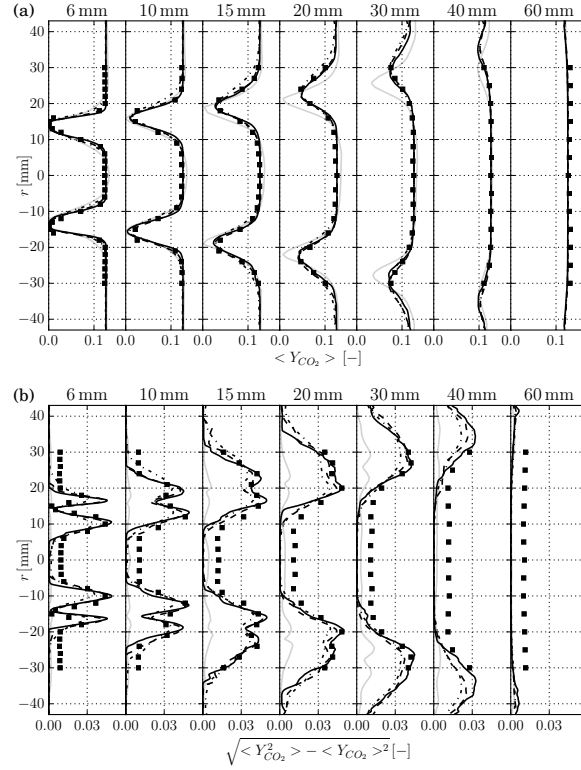


Figure 8: Mean (a) and RMS (b) CO<sub>2</sub> mass fraction profiles for NAD1 (—), NAD2 (-·-·), NAD3 (- - -), NAD4 (—) cases and experiment (■).

the experiment profiles are retrieved only for the inner flame. The dynamics in the non-adiabatic cases is well reproduced with less fluctuations for the outer flame front. NAD4 shows the best agreement to the experiment.

Figure 11 compares the OH-LIF measurements to instantaneous OH concentrations on AD3, NAD3 and NAD4 cases. It is observed that the intermediate species OH is produced in the reaction zone and almost entirely destroyed in the post-flame area. In the non-adiabatic case, no gradient of the OH mass fraction is found in the ORZ as in the experiment. Moreover,

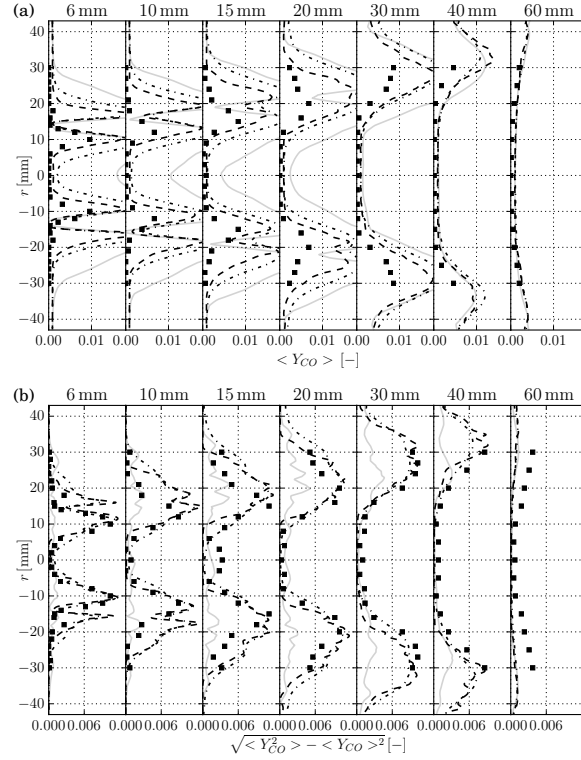


Figure 9: Mean (a) and RMS (b) CO mass fraction profiles for AD1 (—), AD2 (-·-·-), AD3 (- - -) cases and experiment (■).

the NAD4 case seems to have the best agreement in terms of flame wrinkling and spatial distribution of OH mass fraction gradient compared to the experiment.

The outer flame front extinction is now analyzed by introducing the local enthalpy defect  $\Delta H = H - H_{\text{ad}}$  where  $H$  and  $H_{\text{ad}}$  are the local total enthalpy and the total enthalpy of the adiabatic mixture, respectively. A 2-D longitudinal cut of the NAD4 case colored by the instantaneous value of  $\Delta H$  is shown in Fig. 12 and confirms that the slow characteristic time

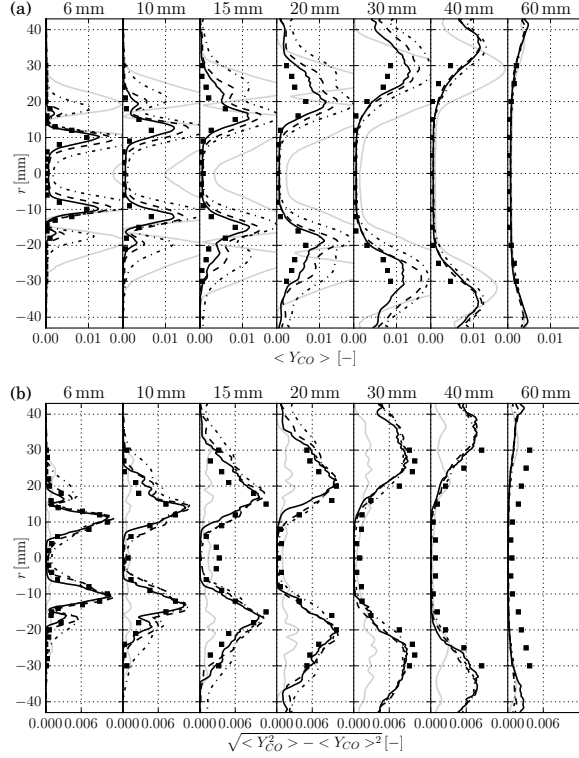


Figure 10: Mean (a) and RMS (b) CO mass fraction profiles for NAD1 (—), NAD2 (-·-·-), NAD3 (- - -), NAD4 (—) cases and experiment (■).

scale of the ORZ promotes heat exchange at the burner walls and causes a drastic fall of total enthalpy in this region. The impact of the enthalpy defect on the outer flame structure is analyzed in Fig. 13 by plotting, for the NAD4 case, a scatter-plot of the heat release rate  $\dot{\omega}_T/\mathcal{F}$  conditioned to  $c \in [0.75 - 0.8]$  against the velocity gradient norm  $|\nabla \mathbf{u}|$ . The velocity gradient is used here as an indicator of the local strain rate seen by the flame front and each point is colored by its local enthalpy defect. Red points corresponds to adiabatic zones while the level of heat loss increases for colors

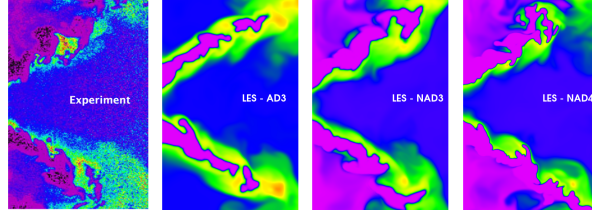


Figure 11: Comparison of OH – LIF measurements to instantaneous OH normalized concentration from LES cases. From left to right: experiment, AD3, NAD3 and NAD4 cases. Colormap: ■ 0.0 ■ 0.25 ■ 0.5 ■ 0.75 ■ 1.0.

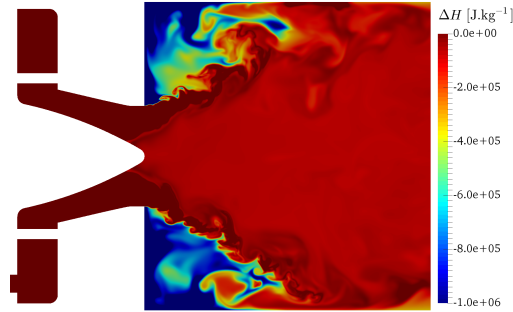


Figure 12: Instantaneous enthalpy defect on the mid-plane for NAD4.

reaching dark blue. Three main zones can be identified: *(i)* A high density of red points (adiabatic) is located at high heat release rates ( $\dot{\omega}_T/\mathcal{F} > 2.10^9$  W.m<sup>3</sup>): they mainly belong to the internal flame front which remains adiabatic and correspond to  $|\nabla\mathbf{u}| \in [10000; 15000]$  s<sup>-1</sup>; *(ii)* A low density of blue points (high enthalpy defect) is located at moderate heat release rates ( $\dot{\omega}_T/\mathcal{F} \in [1.10^9; 2.10^9]$  W.m<sup>3</sup>): they correspond to the reactive outer flame front which is subjected to heat loss and a similar velocity gradient as the inner flame front; *(iii)* A high density of blue points (high enthalpy defect) is located at the bottom of the figure ( $\dot{\omega}_T \approx 0$ ) and corresponds to higher

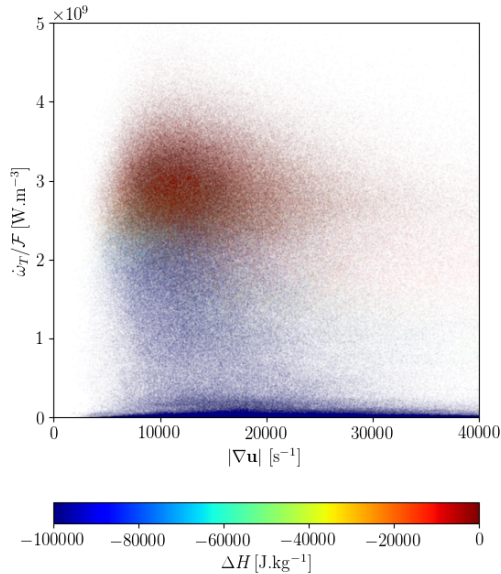


Figure 13: Scatter plot of the heat release rate against the velocity gradient norm, for points with  $c \in [0.75 - 0.8]$ , colored by the enthalpy defect for NAD4 simulation.

values of  $|\nabla\mathbf{u}| \in [10000; 40000]$  s<sup>-1</sup>: they correspond to the quenched outer branch where mixing between adiabatic fresh gases and cooled burnt gases occurs without chemical activity. Interestingly, for the same levels of  $\Delta H$  and  $c$ , (ii) and (iii) exhibit both reacting and quenched flame fronts suggesting that enthalpy defect is not the only physical phenomenon controlling the flame quenching process. However, considering both strain rate (estimated here through  $|\nabla\mathbf{u}|$ ) and enthalpy defect  $\Delta H$  allows to clearly discriminate the reacting points with low strain rates (ii) and quenched points with higher strain rates (iii). The increase of the LOH shown in Tab. 3 is therefore due to higher resolved strain rates on the refined grids leading to an increase of the quenched flame surface. This conclusion is in line with previous studies

performed on counterflow flame configurations [28] showing that burnt gases enthalpy defect decreases the resistance of premixed flame fronts to large strain rates.

## 5. Conclusions

In this work, a numerical strategy to take into account wall heat loss on the lean premixed methane-air PRECCINSTA burner has been proposed. This methodology relies on high-fidelity LES, a skeletal kinetic scheme, the DTFLES model and a wall temperature Dirichlet boundary condition. The results were compared to adiabatic computations and to experimental data. Different grid resolutions were tested, with meshes containing from 1.7 up to 877 millions of elements. The results show that the flame structure is strongly affected by the wall heat transfer whatever the grid size. The enthalpy defect in burnt gases enhances the sensitivity to local strain rate leading to quenching of the outer flame front and changing the flame topology to a V-shape. The temperature and CO distributions are then highly affected. The non-adiabatic case with the most refined grid shows the best agreement to experimental results. Indeed, the V-shape flame structure, the front wrinkling, the temperature and species profiles as well as OH distribution are recovered, confirming the importance of taking into account wall heat loss and complex chemistry effects in such configuration. These results may further be used to develop a sub-grid model closure able to accurately capture intermediate species.

## Acknowledgments

This work was granted access to the HPC resources from CINES under the allocations A0032B06880 made by GENCI and from CRIANN under the allocation 2012006.

## References

- [1] T. Poinsot, D. Veynante, Theoretical and numerical combustion, RT Edwards, Inc., 2005.
- [2] N. Syred, J. Beer, *Combust. Flame* 23 (2) (1974) 143–201.
- [3] R. Mercier, P. Auzillon, V. Moureau, N. Darabiha, O. Gicquel, D. Veynante, B. Fiorina, *Flow, Turbul. Combust.* 93 (2014) 349–381
- [4] G. Lartigue, U. Meier, C. Berat, *Appl. Therm. Eng.* 24 (11) (2004) 1583–1592.
- [5] V. Moureau, P. Domingo, L. Vervisch, *Combust. Flame* 158 (7) (2010) 1340–1357.
- [6] B. Franzelli, E. Riber, L. Y. M. Gicquel, T. Poinsot, *Combust. Flame* 159 (2) (2012) 621–637.
- [7] B. Franzelli, E. Riber, B. Cuenot, *C. R. Mec.* 341 (1-2) (2013) 247–256.
- [8] W. Meier, P. Weigand, X. R. Duan, R. Giezendanner-Thoben, *Combust. Flame* 150 (1-2) (2007) 2–26.
- [9] P. Weigand, X. R. Duan, W. Meier, U. Meier, M. Aigner, C. Brat, *Proc. of the European Combustion Meeting*, 2005, p. 235.

- [10] S. Roux, G. Lartigue, T. Poinsot, U. Meier, C. Brat, *Combust. Flame* 141 (1-2) (2005) 40–54.
- [11] V. Moureau, P. Minot, H. Pitsch, C. Brat, *J. Comput. Phys.* 221 (2) (2007) 600–614.
- [12] B. Fiorina, R. Vicquelin, P. Auzillon, N. Darabiha, O. Gicquel, D. Veynante, *Combust. Flame* 157 (2010) 465–475.
- [13] P. Wang, J. Frhlich, U. Maas, Z. Hea, C. Wang, *Combust. Flame* 164 (2016) 329–345.
- [14] J. M. Lourier, M. Sto hr, B. Noll, S. Werner, A. Fiolitakis, *Combust. Flame* 183 (2017) 343–357.
- [15] V. Moureau, P. Domingo, L. Vervisch, *C. R. Mec.* 339(2/3) (2-3) (2011) 141–148.
- [16] A.J. Chorin, *Math. Comp.* 22 (1968) 745–762.
- [17] C. D. Pierce, P. Moin, *J. Fluid Mech.* 504 (2004) 73–97.
- [18] M.Kraushaar, Ph.D.thesis, CERFACS (2011).
- [19] R. Yu, J. Yu, X.-S. Bai, *J. Comput. Phys.* 231 (16) (2012) 5504–5521.
- [20] S. D. Cohen, A. C. Hindmarsh, *Comput. Phys.* 10 (2) (1996) 138–143.
- [21] P. Benard, V. Moureau, G. Lartigue, Y. DAngelo, *Int. J. Hydrogen Energy* 42 (4) (2017) 2397–2410.

- [22] R. Sankaran, E.R. Hawkes, J.H. Chen, T. Lu, C.K. Law, *Proc. Combust. Inst.* 31 (2007) 1291–1298.
- [23] G. Smith, D. Golden, M. Frenklach, N. Moriarty, B. Eiteneer, M. Goldenberg, C. Bowman, R. Hanson, S. Song, W. Gardiner, et al., Technical Report, Gas Research Institute (1999).
- [24] M. Germano, U. Piomelli, P. Moin, W. H. Cabot, *Phys. Fluids A* 3 (7) (1991) 1760–1765.
- [25] O. Colin, F. Ducros, D. Veynante, T. Poinso, *Phys. Fluids* 12 (7) (2000) 1843–1863.
- [26] F. Charlette, C. Meneveau, D. Veynante, *Combust. Flame* 131 (2002) 181–197.
- [27] M. Cailler, R. Mercier, V. Moureau, N. Darabiha, B. Fiorina, 55th AIAA Aerospace Sciences Meeting, AIAA 2017-0606 (2017).
- [28] B. Coriton, M.D. Smooke, A. Gomez, *Combust. Flame* 157 (11) (2010) 2155–2164

**Supplemental Material**

[Click here to download Supplemental Material: SupplementaryMaterial.pdf](#)

LaTeX 2 Column File

[Click here to download LaTeX 2 Column File: main\\_2column.pdf](#)